IN SITU TRIBO-ELECTROCHEMICAL CHARACTERIZATION OF DIAMOND-CONTAINING MATERIALS

A Dissertation

by

HUAPING XIAO

Submitted to the Office of Graduate and Professional Studies of
Texas A&M University
in partial fulfillment of the requirements for the degree of

DOCTOR OF PHILOSOPHY

Chair of Committee,	Hong Liang
Committee Members,	Timothy J. Jacobs
	Alexei. V. Sokolov
	Partha P. Mukherjee
Head of Department,	Andreas A. Polycarpou

August 2014

Major Subject: Mechanical Engineering

ABSTRACT

Diamond has been under spotlight in industry since the discovery of its extraordinary mechanical properties, high wear resistance and excellent chemical inertia. These properties enable diamond a competitive candidate for industrial and biomedical applications. In the present research, the tribological properties of two types of diamond materials, diamond reinforced ceramic composites and diamond coatings have been investigated.

Experimental approaches consist of tribological investigation, electrochemical evaluation and characterization of diamond-reinforced ceramic composites (DRCC), thin nanocrystalline diamond (NCD) film, thin microcrystalline diamond (MCD) film and their functionalized derivatives.

After the tribotest, phase transformation from diamond carbon (sp^3) to amorphous carbon (sp^2) is confirmed by Raman spectroscopy in the diamond composite. The surface roughness of the diamond grits was found to be greatly reduced due to wear. A tribo-electrochemical method is developed to *in situ* monitor the this amorphrization-wear process. It is discovered that the current density is a function of the excitation voltage in a sinusoidal pattern. The amplitude and period of the sinusoidal pattern reflect the intensity and the frequency of the process. For the diamond-cartilage contact, it is found that the coefficient of friction between cartilage Figure and diamond decreases with increasing load because real contact area is not

linearly change with load. Even though the hydrogen treatment decreases the friction and ammonia treatment decreases adhesion and friction in dry conditions, the friction under lubrication is determined by synergy effects of number of bonds established and strength of single bond between protein of the cartilage and the diamond surface.

In the present research, the wear mechanism of diamond-reinforced composite has been demonstrated. The amorphization-wear process of diamond can be real-timely monitored using electrochemical approach. The frication force between diamond surface and human cartilage can be adjusted by changing number of bonds established or strength of single bond between protein of the cartilage and the diamond surface. This research proposes new avenue in the evaluation of friction and wear of diamond materials, which will be beneficial to wide range of diamond applications, including aerospace industries, mechanical processing, biomedical science, prosthetics and energy industries.

DEDICATION

To my beloved family for encouraging me and supporting me as always. To my advisor, Dr. Liang, for making me confident and optimistic.

ACKNOWLEDGEMENTS

Completing the study and research for this Ph.D. degree has been both a challenge and a fulfillment for me. I have received the support and assistance from many people in this period. It would be much harder for me to work through without their kind and generous help if it is not impossible.

First of all, I would like to thank my committee chair, Dr. Hong Liang, for her constant support, encouragement and guidance all through the three years in Texas A&M University. My critical thinking, writing skills for scientific manuscript, and the ability of conceiving creative ideas have been greatly improved with her instruction. I would also like to thank my committee members, Dr. Timothy J. Jacobs, Dr. Alexei. V. Sokolov, and Dr. Partha P. Mukherjee, for their support and valuable suggestions throughout the course of this research.

I am particularly grateful to the financial support from Texas A&M University, Texas Engineering Experiment Station, Baker Hughes, and Kennametal, Inc.. The gratitude also goes to the Physics Department and the Microscopy Image Center (MIC) at Texas A&M University for their materials characterization service.

I also want to acknowledge all the members in Surface Science Group for their generous assistance, helpful advices and precious time for discussion in my study and research. Assistance provided by Dr. Chih Lin, Dr. Hung-Jue Sue, Dr. Alexander Sinyukov, Mr. Miao Song, and Mr. Peng Li is also appreciated.

Thanks also go to my friends and the department faculty and staff for making my time at Texas A&M University a great experience.

Finally, I would like to express my gratitude to my parents, my wife, and other family members for their support, encouragement, and endless love.

NOMENCLATURE

Acronyms

AFM	Atomic force microscope
CMP	Chemical mechanical polishing
CPE	Constant phase element
CVD	Chemical vapor deposition
DLC	Diamond like carbon
DRCC	Diamond-reinforced ceramic composite
ECMP	Electro-chemical mechanical polishing
EIS	Electrochemical impedance spectroscopy
MCD	Microcrystalline diamond
MPCVD	Microwave plasma chemical vapor deposition
NCD	Nanocrystalline diamond
PCD	Polycrystalline diamond
PVC	Polyvinylchloride
SEM	Scanning electron microscope
TEM	Transmission electron microscope/microscopy
UNCD	Ultrananocrystalline diamond

Symbols

a	Amplitude of fluctuation pattern
Ar	Real contact area
i	Current density
N	Applied load
T	Period of fluctuation pattern
V	Potential
θ	Phase shift

TABLE OF CONTENTS

Page

LIST OF FIGURES

Page

LIST OF TABLES

Page

CHAPTER I

INTRODUCTION

In this chapter, essential knowledge and information will be provided for readers to understand the background of current research. This research focuses on tribological performance of diamond containing materials. Properties of these materials, their applications in mechanical and biomedical fields, basics of wear and current problems will be briefly introduced.

1.1. Basics of diamond

Diamonds are commonly regarded as gemstones and popularly utilized for components in jewelry. The productivity of diamond has been greatly increased since the synthetic method was developed to generate diamond from other forms of carbon. The applications of diamond materials expanded to manufacturing and processing industry due to their extremely high hardness and strength. Later, more and more interesting properties of diamond, such as low friction, chemical inertness, high thermal conductivity and excellent biocompatibility, were discovered and investigated, making diamond a popular player in scientific research. In this section, the structure and properties of diamond will be reviewed.

1.1.1. Atomic structure of cubic diamond

Diamond is composed of carbon atoms with a tetrahedral arrangement. One unit cell of cubic structured diamond is illustrated in Figure 1.1. The carbon atoms form a varied arrangement of face-centered cubic structure. There are four more atoms (red) inside the unit cell besides eight atoms (green) at the corner and six atoms (purple) in the center of the face plane. In each unit cell, there are 4+8*1/8+6*1/2=8 atoms. This crystal structure is termed as diamond lattice. In this structure, each carbon atom is coordinated to four adjacent carbon atoms with a tetrahedral arrangement. The center atom is connected to the atoms at the four corners by sp^3 bond, a particular type of covalent bond according to hybrid orbital theory. The lattice constant of the diamond cubic is 0.357 nm and the length between two neighboring carbon atoms is 0.154 nm.

Both graphite, which is the mostly seen form of carbon, and diamond are compose of pure carbon. The hardness and strength of diamond, however, are much higher than those of graphite. Graphite has a layered structure as shown in Figure 1.2. In the plane, carbon atoms are sp^2 bonded in a hexagonal arrangement. However, between two layers there is no strong atomic bond and they are connected by Van der Waals force. This force is a much weaker interaction so the adjacent planes can easily slide over each other. This is the reason why graphite is widely used as solid lubricant.

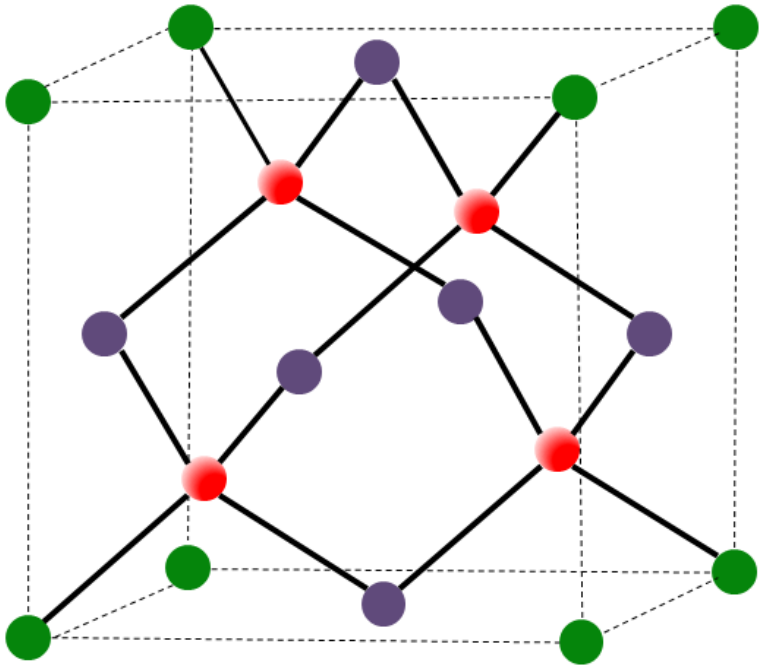

Figure 1.1. Atomic structure of cubic diamond (lattice constant is 0.357 nm).

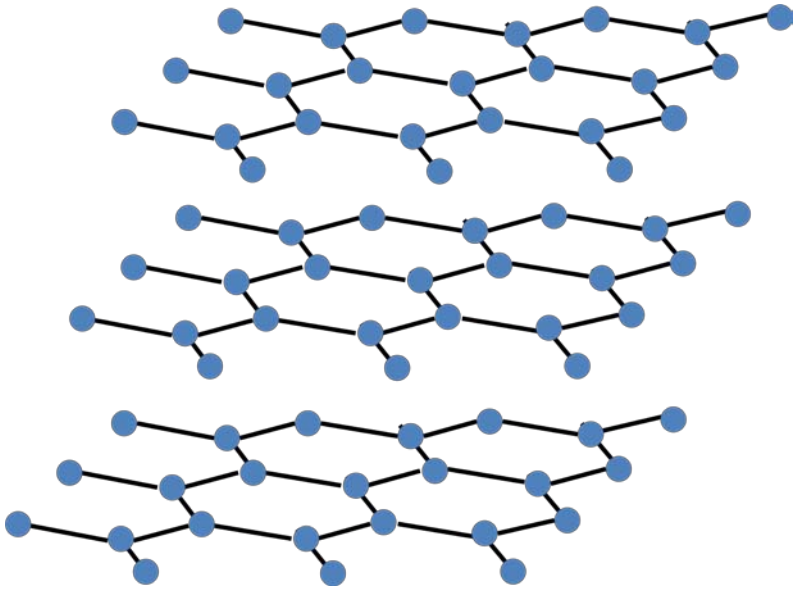

Figure 1.2. Layered structure of graphite.

1.1.2. Man-made diamond

In this section, different technologies developed to produce diamond will be discussed. The production of diamond greatly increased after the invention of apparatus forming man-made diamond. With the development of these technologies, both the quality and size of synthesis diamond have been improved. As a result, nowadays, the amount of man-made diamond is about 3 times higher than that of natural diamond from mining,[1, 2] making it the major source of raw materials for diamond containing components.

1.1.2.1. Single crystal diamond

Single crystal diamonds are the most common forms of diamond found in natural environment. They are formed from carbonaceous materials at extremely high temperatures and pressures. The location for diamond formation is usually more than one hundred kilometers under the ground.[3] The diamonds are carried from deep mantle to the earth surface by the volcano activity.

Hard work has been done to produce man-made diamond when the diamond was discovered to be a form of carbon.[2] Different types of reactions were explored to generate diamond but only one of them showed positive results. At controlled and stable temperatures and pressures, diamond crystallize from carbon dissolved in molten metals, such as nickel and iron.[1] Figure 1.3 schematically illustrates the formation of diamond in a high pressure chamber. Countless attempts had been made

to synthesize diamond before the acknowledged success of General Electric Co. in 1955.[4] The researches utilized a "belt" apparatus which was able to reach higher than 41 GPa and 5000 ^{o}C at the same time.[5] The development of diamond synthesis was greatly improved immediately after the first successful attempt was made. Giardini et al.,[6] Hall,[7, 8] Wedlake,[9] and Pugh et al.[10] developed various experimental devices to produce diamond from carbonaceous materials, most of which are graphite, in terms of high pressure synthesis.

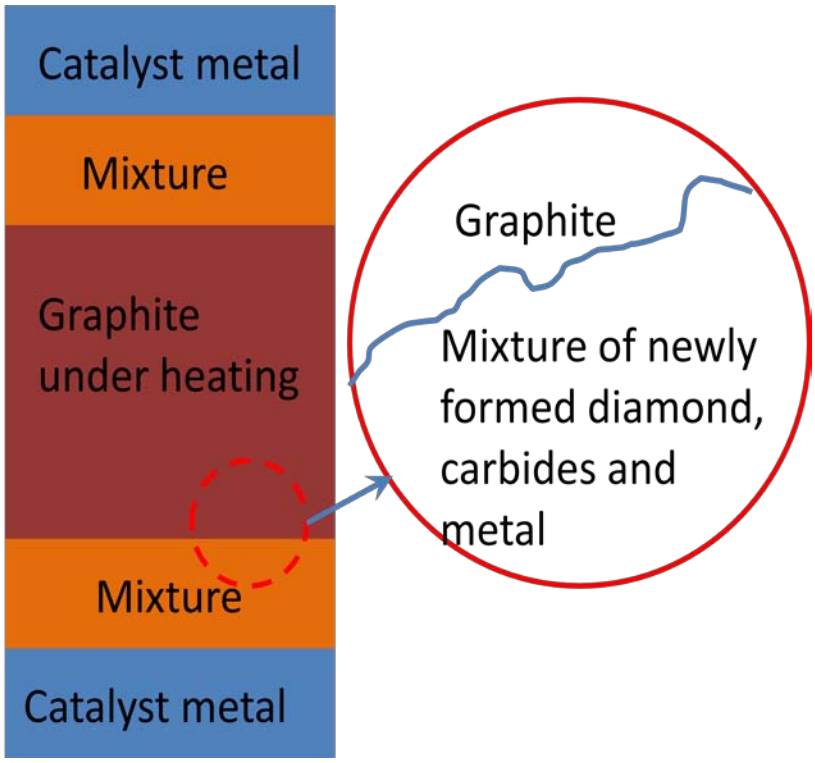

Figure 1.3. Schematic of formation of diamond under high pressure and high temperature.

In addition to high pressure synthesis method, shock wave process is another approved approach to produce single crystalline diamond. Very small diamond particles were obtained by DeCarli and Jamieson in 1961.[11] A shot shock wave was believed to generate extremely high pressure up to 60 GPa when they applied an explosive charge to graphite. Their work was followed by Sekine et al.,[12] Simonsen et al.,[13] Trueb[14-16] and others.[17, 18] The exact mechanism of the shock synthesis process is still under exploring. One possible explanation is that the shock generates high temperature and high pressure, melting the graphite and converting graphite into diamond. The reaction occurs in a very short time interval and then the pressure drops rapidly, leading to the reconversion of diamond back to graphite.[2] Due to this effect, the diamond phase formed by shock wave is not stable and the productivity is relative low.

1.1.2.2. Polycrystalline diamond

Compared to single crystalline diamond, polycrystalline diamond (PCD) is harder and tougher in texture. With the rigid atomic structure, single crystalline diamond is relatively weak in particular cleavage direction. In PCD, the growth direction of each grain is randomly distributed. As a consequence, the development of dislocation or crack stops at the boundary of two grains. This effect determines that PCD is tougher than single crystalline diamond. Reduced population of dislocation and plastic deformation due to grain boundary also increases the hardness of PCD. The

featured Raman peaks for single crystalline diamond, nanocrystalline diamond (NCD) and microcrystalline diamond (MCD) are shown in Figure 1.4. A sharp peak at 1333 cm^{-1} can be determined in single crystalline and MCD. This peak is the featured peak for sp3 bond between carbon atoms. For MCD, D band between 1200 cm^{-1} to 1400 cm^{-1} for disorder carbon (sp^2 bonded) is also detected in addition to the sharp peak. In the spectrum of NCD, there is no sharp peak observed. Three broad bands are observed at 1136 cm^{-1}, 1333 cm^{-1}, and 1587 cm^{-1}. The D (1333 cm^{-1}) and G (1587 cm^{-1}) bands are related to sp^2 bond and are detected in Raman spectrum due to the grain boundary in NCD structure.[19] It is concluded that in single crystalline diamond all carbon atoms are sp^3 bonded. In PCD, such as nanocrystalline diamond and microcrystalline diamond, the concentration of sp^3 bond decreases and sp^2 bond is dominating. Using Raman spectroscopy, various types of diamonds can be easily distinguished.

It is very difficult to obtain PCD from natural source. Various approaches have been developed to produce PCD. An early experiment performed by Wentorf et al.[20] in 1980 successfully generated PCD film from tiny diamond particles. These diamond particles were sintered under high temperature and pressure, which are relatively lower than those for diamond synthesis.

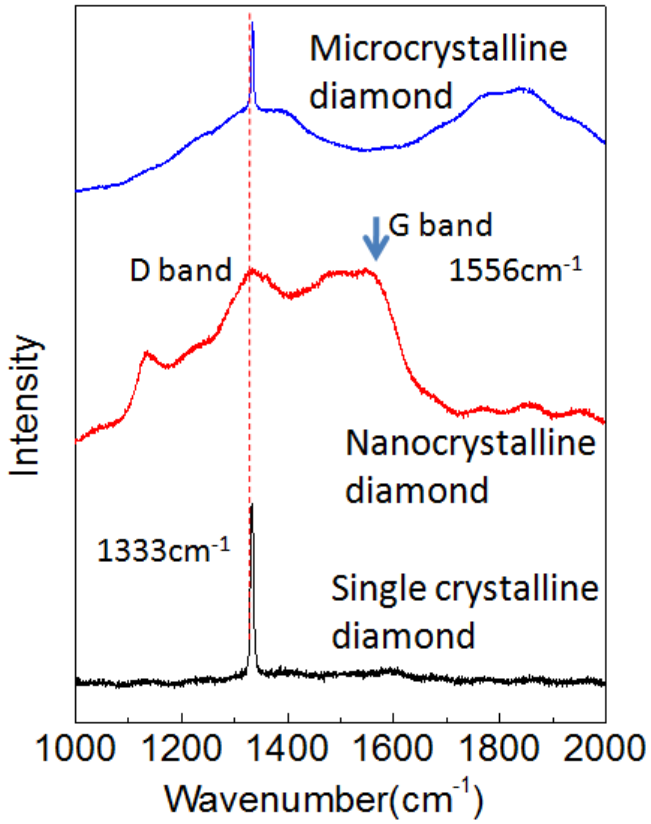

Figure 1.4. Raman features for single crystalline diamond, nanocrystalline diamond and microcrystalline diamond.

The sintering of diamond is schematically described in Figure 1.5. The mixture is heated to a temperature at which approximately 70% of the melting temperature of diamond under high pressure. The catalyst metal, such as cobalt, melts and prevents the transformation of diamond to graphite during sintering process.[21-23] The sintering method for producing PCD have been modified and improved later. Big bulk of PCD

(disc with a diameter of 50 mm and thickness of 5 mm [1]) could be produced using sintering technology.

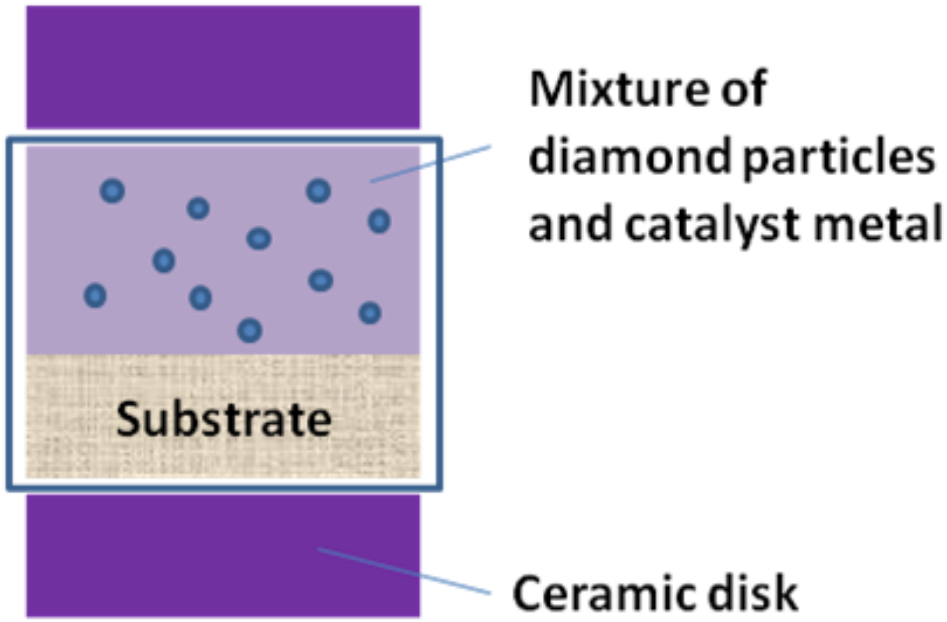

Figure 1.5. Schematic description of PCD sintering.

In many cases, only a thin coating film of PCD on the substrate is necessary to modify interface properties. Chemical vapor deposition (CVD) is the most commonly utilized approach to produce thin PCD films in nano and micro scale. Compared to the high temperature and high pressure technologies discussed above, deposition of diamond can be achieved at a much lower pressure using CVD. The principle of diamond CVD is schematically illustrated in Figure 1.6. The carbon source of diamond

is methane. Hydrogen is usually included in the gas source for chemical reactions. The ratio of methane to hydrogen varies from case to case depending on the diamond types. There are three primary stages involved in the diamond CVD. External energy source, such as microwave, direct current, and hot filament,[24-39] produces a plasma in the reaction chamber to activate the mixture of gas. Under the effect of plasma, the gaseous materials are heated up to a temperature over 1000 ^{o}C. Bonds between atoms are broken down and the gas molecules are converted into active particles like radicals, ions and electrons as shown in Figure 1.6. In the second stage, a set of complicated chemical reactions occur between these reactive particles until they finally reach the substrate. The fragments involved in these reactions are moved and circulated by the gas flow and diffusion. In the final stage, the gaseous species near the substrate forms a diffusion layer and reacts with the surface. At the interface, various reactions and processes occur, including adsorption of the active particles onto the surface, desorption of them back to the diffusion layer, transportation of them from one region to another for suitable reaction site. Diamond is deposited on the substrate through these complex reactions. An accurate evaluation of chemical reactions in diamond CVD is not available. Different factors, diffusion temperature, types and ratios of gaseous phase, surface structure of substrate, types of energy source, greatly impact the growth of diamond, making it even harder to study.[40, 41]

The diamond CVD has been widely studied since in the produce of diamond was possible.[42, 43] Numerous modifications and improvements have been introduced by

subsequent researchers.[25, 43-48] To date, these techniques have been widely applied to produce polycrystalline diamond.

1.1.3. Properties of diamond

In this section, main properties of diamond will be discussed. These properties determine the wide applications of diamond materials in both industrial and scientific fields.

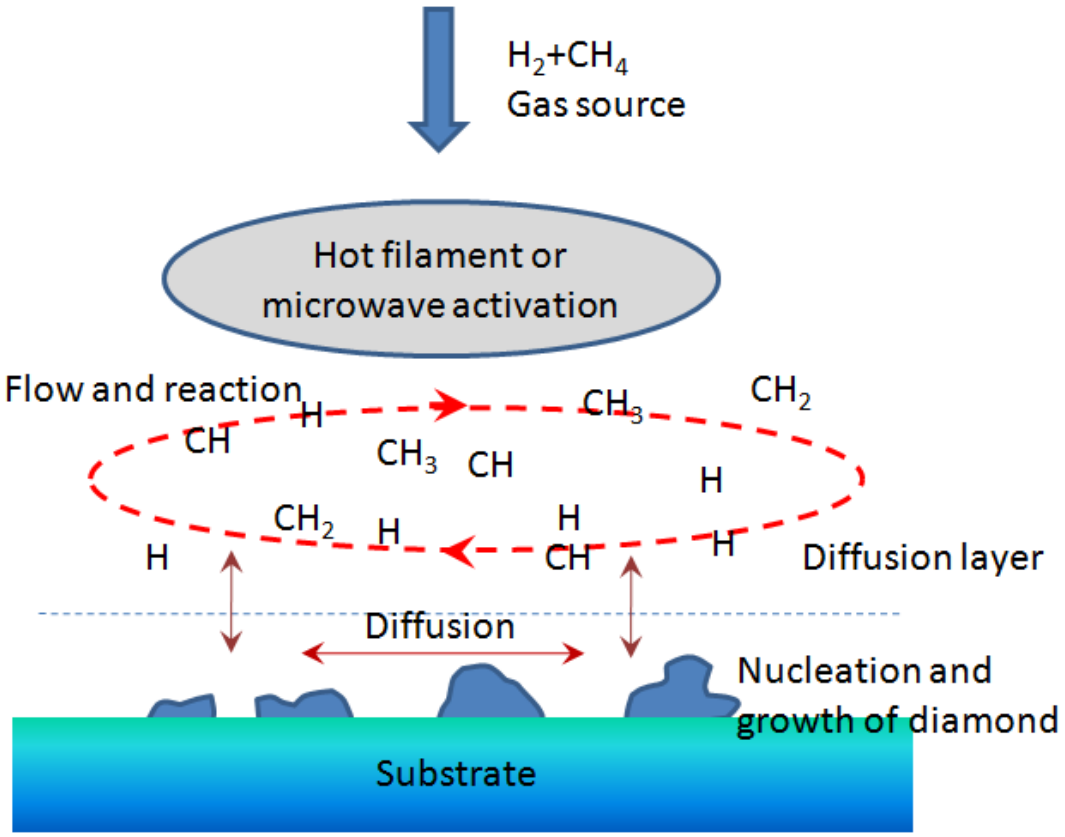

Figure 1.6. Diamond CVD process.

1.1.3.1. Hardness

Hardness is used to evaluate the resistance of a material to plastic deformation under external force. The higher hardness of a material is, the harder it is to force the material deform permanently. Diamond is well known for its highest hardness of all recognized materials. In the Mohs scale of hardness for mineral ranging from 1 (the softest) to 10 (the hardest), diamond has the highest value of 10. Even though many novel super hard materials have been fabricated,[49-53] none of them have been proven to be superior to natural diamond in hardness. Due to this property, diamond is usually employed as sharp indenters to produce indents on other materials as the criterion of hardness measurement.

1.1.3.2. Thermal conductivity

The measured thermal conductivity of diamond is 900–2,320 $W \cdot m^{-1} \cdot K^{-1}$.[54-56] This value remains unbeatable among currently known materials. The thermal conductivity of diamond could be greatly improved when the isotopic purity of ^{12}C is increased from 98.9% (the natural concentration) to 99.9%.[54] In some MEMS or semiconductor devices where extreme heat dissipation ability is required, thin diamond film is utilized.[57-59]

1.1.3.3. Young's modulus

Modulus is a measure to evaluate the resistance of a material to elastic

deformation. According to Hooke's law, the modulus can be easily obtained from the stress strain curve by calculating the slope of the curve in elastic region. The measured modulus of single crystalline diamond is 1050 GPa[60] and that of polycrystalline diamond is 500-533GPa.[61] The modulus of diamond is higher than that of most other materials. Carbyne, another allotrope of carbon was reported to have the highest elastic modulus of 32700 GPa in all the materials.[62]

1.1.3.4. Chemical stability

Diamond is chemically inert. At a high temperature of 625 °C, a graphite-like layer was found on the diamond surface in oxygen environment, indicating the oxidation of diamond.[2] Diamond and carbon dissolve in some molten metals, such as Fe, Ni, Mg, and Co, at higher temperature.[63] At room temperature diamond has excellent resistance to any chemical attacks even from strong bases and acids. Based on this fact, the impurities on the synthetic diamond surface can be removed by those reaction agents.

1.1.3.5. Tribological properties

The tribological properties of diamond have been partially revealed. Low friction was found in diamond or diamond-based structures, including diamond like carbon (DLC) films,[64, 65] ultrananocrystalline diamond,[66] doped DLC film,[67, 68] among others. The study of low friction diamond[69-71] could improve the performance of

contact surface in mechanical components and reduce the energy loss due to friction. The potential application of diamond-based micro electromechanical systems has been established duo to the study of surface features of diamond thin films in nano-scale.[72-75] In vacuum environment, COF on diamond surface jumps fast to approximately 1.[76] More detailed information on tribological properties of diamond will be discussed later.

1.1.3.6. Biocompatibility

The excellent biocompatibility of diamond and diamond-like carbon has been experimentally approved. Variety of studies on determining biological impacts of diamond materials have been performed by means of in vitro or in vivo tests.[77-84] The results demonstrate that diamond materials are adherent to types of bio tissues and no toxic effects are detected. Most diamond materials are chemically composed of biologically compatible elements, namely carbon, nitrogen and hydrogen. As a result, these materials show positive results in biocompatibility measurements.

1.1.4. Applications of diamond

Diamond has been under spotlight since the discovery of its extraordinary mechanical and tribological properties. The excellent hardness, stiffness, and tribological performance enable diamond a competitive candidate where low friction and reliable wear resistance is desired. In this section, applications of diamond materials in various

areas will be reviewed.

1.1.4.1. Diamond tools for processing and machining

All other materials have lower hardness than diamond. Theoretically, diamond materials can be used to machine any materials except for itself. Deposition of a diamond layer on ordinary cutting tools can remarkably decrease the wear and prolong the service life.[85] PCD blocks have been widely used as inserts in drilling and turning tools.[86-98] Davim and Baptista[90] investigated the cutting force using PCD tools to machine silicon carbide reinforced aluminum. They found that the cutting force in turning gradually and progressively increases with time during machining. Huang et al.[99] used PCD tools to process SiCp/Al composites, which is a promising material with outstanding thermo-physical performance but its machinability is poor. The quality of the finished surface was found to increase with machining speed. Andrewes et al.[100] utilized PCD inserted cutting tool to machine SiC-reinforced aluminum and results revealed that combination of good thermal conductivity and low COF led to wear of diamond. The performance of brazed PCD tool in processing metal-based composites was evaluated by Davim.[101] It was demonstrated that it is necessary to use diamond tool to machine SiC reinforced metal-based composites in order to ensure long tool life.

In addition to PCD, single crystalline diamond grits are usually employed as reinforcements in grinding and sawing tools. Guo et al.[102] investigated the performance a set of diamond grinding wheels on grinding optical class. It was demonstrated that depth

of surface damage if diamond wheel with coarser grains was used. Simulation results from Koshy et al.[103] indicated that the surface roughness of the finished workpiece is related to the distribution of diamond grit protrusion height. Zhao et al.[104] utilized diamond grinding tool to conduct ultra-precision processing. The diamond tool showed extremely low vibration in grinding optical classes. The integrity of surface and surface in ground optical glass was improved and more polishing time could be saved.

1.1.4.2. Diamond tips for scanning or indentation

For the probe measurement and indentation test in micro and nano scale, the key factor is the quality of the tip. In order to obtain reliable and consistent results, it is essential for the tip to maintain the origin shape and surface morphology. This means the material for fabricating tip needs to be resistant to both elastic deformation and plastic deformation. Diamond is the most promising candidate except for its coat considering the requirements in mechanical properties. Due to the extreme hardness and elastic modulus, diamond has been widely used in scanning probes[105-108] and micro and nano indenters.[68, 109-111] Niedermann et al.[112] coated PCD films on silicon AFM tip with a doped layer and investigated the performance of the modified tip in AFM scanning and nanoindentation experiments. The diamond coated tip presented atomic-scale resolution. The obtained results demonstrated that CVD diamond was suitable for manufacturing nanoprobe tools with controlled quality. In addition to the excellent mechanical proprieties, the interesting electrical properties of diamond expand the applications of

diamond in micro and nonoprobe measurements. Gallo et al.[113] employed the diamond tip to image the pore networks structure of ultrafiltration membrane. The utilization of diamond tip in exploring the breakdown voltage, nano-scanning resistance imaging, and investigating electrical properties of WS2 in form of thin films[113] has been reported.

1.1.4.3. Diamond in biological and biomedical applications

As a promising material for biomedical application, diamond have attracted great attention due to its chemical inertness, low friction and high wear resistance. These properties make diamond a promising candidate as coatings materials in biological and biomedical applications. DLC coated Ti specimen was proven to be capable of staying in the muscle of rabbits for approximately one year without obvious negative effect.[114] Chong et al.[115] investigated the cell adhesion properties on diamond surfaces with different functionalizations. It was found that surface oxygenation increases the hydrophilicity and provided a better environment for cell adhesion. Hauert et al.[116] studied the performance of Ti-DLC exposed to a biological environment and discovered that the adsorption of proteins on the sample surface is dependent on the concentration of Ti.

Diamond materials have been proved to be a potential candidate in prosthetics. DLC coating on metal (Co28Cr6Mo) surface was found to effectively reduce the volumetric wear[117] in artificial joint. The wear rate of tetrahedral amorphous carbon (ta-C) coated metal-on-polyethylene mating pair was 10^5-10^6 times lower than the

metal-on-metal or metal-on-polyethylene joint and the corrosion rate greatly decreased as well.[118] The service time of artificial joint has been significantly increased by coating ta-C film on both metal surface and polymer surface for an ultra-high-molecular-weight polyethylene and Co-Cr-Mo contact.[119]

1.2. Friction and wear of material

Friction and wear are two of the primary reasons responsible for energy and mass loss in mechanical systems. Holmberg et al.[120] demonstrated that almost one-third of the energy extracted from fuel is lost due to friction and wear in a car. When two surfaces in contact have relative motion, friction is inevitable even though the surface roughness is very low. In this section, basic knowledge about wear will be introduced. Wear of diamond materials will discussed as well.

1.2.1. Origin of friction and wear

Understanding of origin of friction and wear is the heart of tribology. Modern search on friction and wear mechanism started from 1940s[121-128] based on the platform established by Amontons and Coulomb. With the fast development of nanotechnology, exploring of friction and wear mechanism in nano scale have been progressively carried out.[129-133]

According to those classic theories, friction between two mating surfaces comes from three sources. Two surfaces in contact with relative motion is schematically

presented in Figure 1.7. Figure 1.7 (a) shows a pin-on-disk configuration and Figure 1.7 (b) displays the interface in a smaller scale. For clearer illustration, the contact between two single asperities is shown in Figure 1.7 (c), (d) and (e). The first origin of friction and wear is plastic deformation on the surface as in Figure 1.7 (c). When two surfaces are pressed against each other, plastic deformation is generated on the softer material if the external pressure is high enough to overcome the yield strength. Friction force is the macro scale display of the stress produced in the deformation process.[128, 134] Similar to the case of plastic deformation, friction results from the stress between two asperities when they are elastically deformed as shown in Figure 1.7 (d).[127, 128] Interfacial bonds and reactions are another primary source of friction. In close contact, van der Waals forces increases when the two asperities approaches each other. The formation and breakage in the sliding process produce a tendency of shear and accordingly stress.[135-139] This process is shown in Figure 1.7 (e). Due to the complex surface and interface conditions, the three effects are not independent from each other. In real applications, plastic deformation, elastic deformation and interfacial bonds usually coexist, making the analysis of wear mechanism more complicated. Different wear mechanism lead to various types of wear, which will be discussed in the next section.

1.2.2. Different types of wear

The complex nature of interfacial reaction determines that wear on surface have multiple forms. The Four typical types of wear is illustrated in Figure 1.8.

Abrasive wear happens when a hard surface slides against a softer material under relatively high pressure as in Figure 1.8 (a).[121, 127] The hard asperities scratch off the material on the counter surface and generate macro scale plowing track. The plowing track on worn surface is illustrated in Figure 1.9.

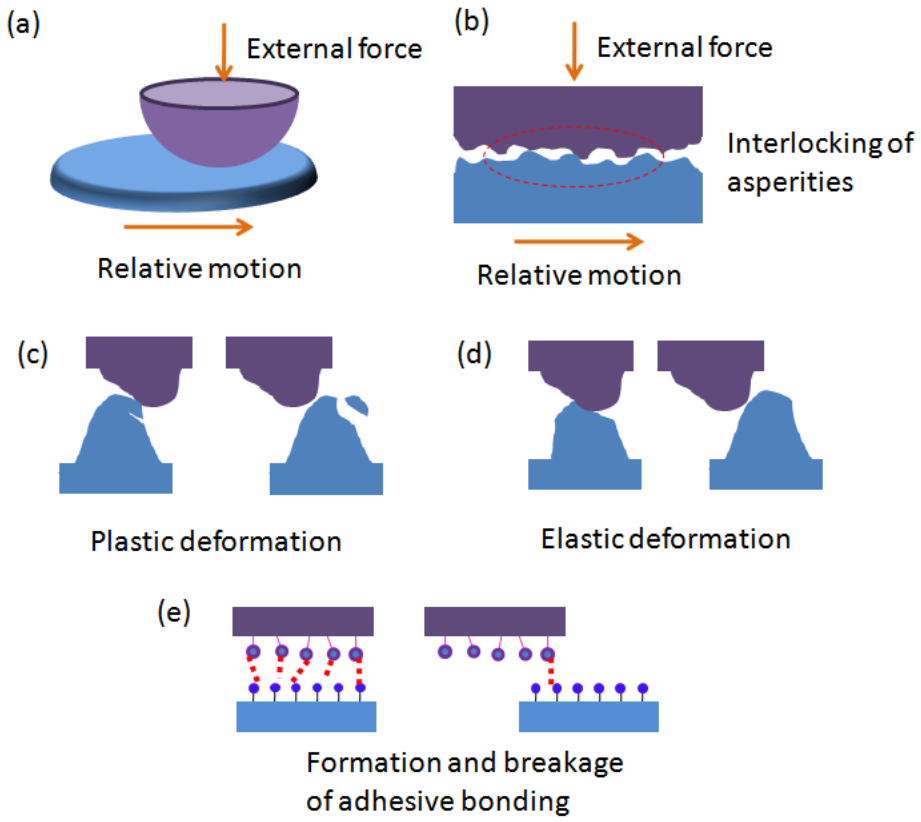

Figure 1.7. Illustration of friction and wear between two surfaces.

Massive amount of heat is generated during the sliding of two surface. The heat is highly localized so the temperate of a particular asperity could be really high, leading

to the softening of the material as in Figure 1.8 (b). There is a chance that the soft portion detaches from the previous surface and attaches to the hard asperity. This produces a material transfer from one surface to another. This process results in the delaminating of the softer material as shown in the red rectangles of Figure 1.9.

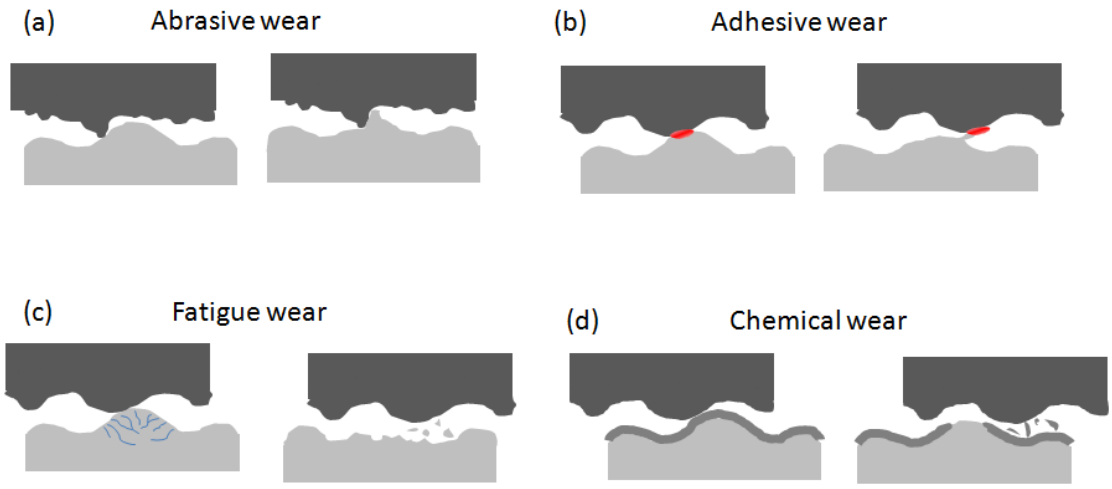

Figure 1.8. Four typical types of wear.

For elastic materials, deformation recovers when the contact separates (Figure 1.7 (d)). As a result, elastic deformation doesn't generate visual wear. However, if the asperity is subjected to cyclic pressure fatigue wear will happen after a long time as in Figure 1.8 (c). In this case, even though the pressure is not high enough to force the material deform plastically, the long lasting cyclic application of load causes fatigue and finally leads to permanent deformation.[140-142]

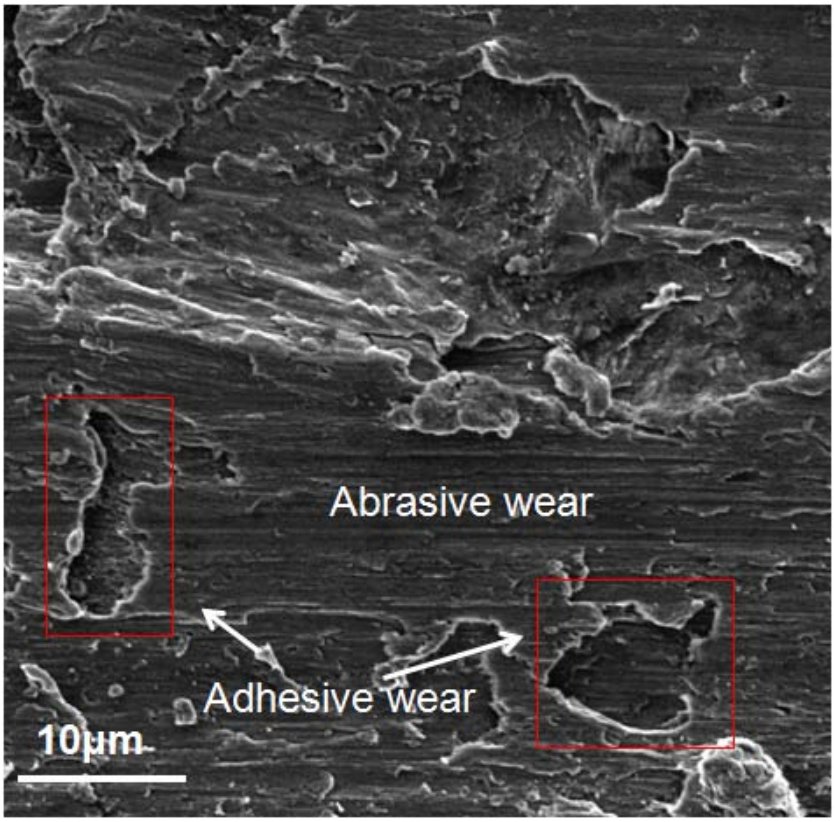

Figure 1.9. Worn surface showing features of abrasive wear and adhesive wear.

In many applications, the mechanical components are exposed to oxygen, chemicals or other reactive agents. Chemical reactions induced change on the surface materials could new substances which are more easily removed as shown in Figure 1.8 (d). As a consequence, the wear on surface increases due the combined effects of chemical reactions and mechanical scratch.[143-146]

1.2.3. Wear of diamond containing materials

Although diamond and DLC are well known for their extraordinary mechanical properties and chemical inertness, they have been found to wear in many industrial applications, such as mining, drilling, machining, or being used as indenters and tips of probe-based profilometry.[65, 67, 68, 73, 147, 148]

In machining process, the friction force between tools and workpieces is extremely high. Tool wear is a common phenomenon even though diamond is superior to all other materials in hardness. In order to evaluate the performance of various machining tool, extensive studies have been conducted. Flank wear was found to be the dominating wear of PCD cutting tools[100, 101] in machining of hard ceramics. Wear of different portions of cutting tool is shown in Figure 1.10. The most observed wear had the features of adhesive wear and abrasive wear. Compared to PCD tools, CVD diamond was reported to have a shorter life.[100] Hu et al.[149] found that delamination was the leading cause of wear of NCD and MCD tools. After polishing, the wear resistance of the diamond cutting tools increased, leading to longer tool life.[150, 151]

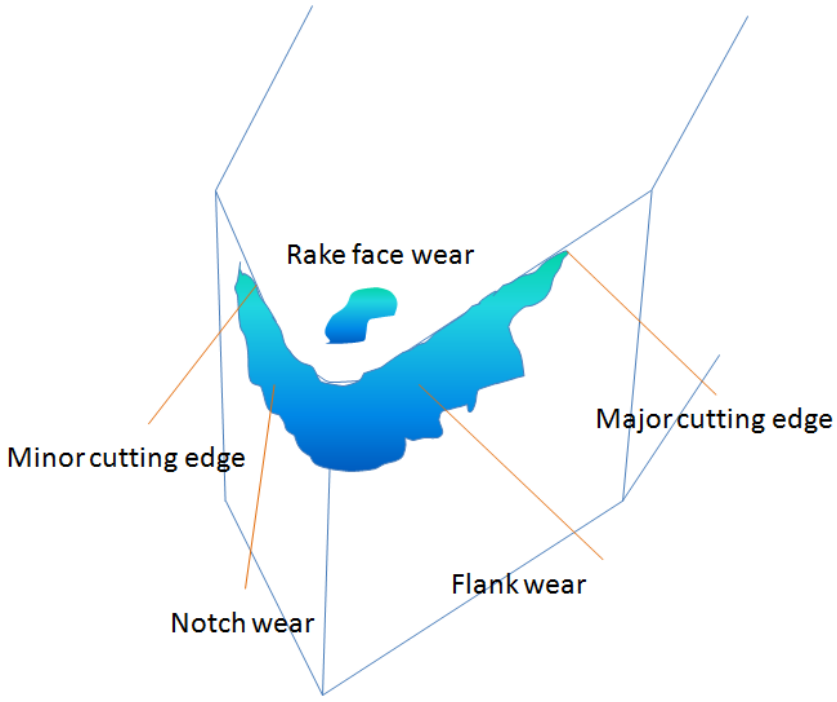

Figure 1.10. Tool wear on diamond cutting tool.

For grinding tools with diamond grits, the primary wear type is attritious wear for conventional grinding.[1, 152] Ding et al.[152] employed ultrasonic vibration-assisted grinding to process SiC and they found that macro and micro fracture of the diamond grits was the dominating factors leading to wear. Hitchiner and Wilks[153] used diamond tools to machine hard metals, such as tool steels and stainless steels. The experimental results showed that chemical wear of diamond grits induced by oxidation often played important role in grinding.

In scanning and indentation process, friction between probe tip and sample surface is inevitable. Actually, friction induced wear is one of the most common

reasons for failure of the probe.[154] Wear of probes is one of the major concerns of researches because damage or deformation of probes resulted from wear reduce the precision of measurements and tests. Liu et al.[155] fabricated an ultrananocrystalline diamond (UNCD) probe for AFM scanning. In subsequent experiment, the UNCD probe showed much better wear resistance than the conventional silicon nitride probe. Both abrupt fracture and slowly grown wear were found in a diamond coated AFM probe by Chung and Kim.[154] In addition to fracture and gradual wear, Liu et al.[156] demonstrated that the adhesive force led to the damage and wear of probe. Kim et al.[67] confirmed this statement. In their experiment with UNCD probe, the domination wear mechanism was the detach of grain from the probe rather than surface atoms erosion.

1.3. Monitoring of wear

Great attention has be paid to study the friction and wear of diamond containing materials. Exploring how wear happens and understanding the wear mechanism are key to improve the performance and prolong the service life of these materials. In this section, approaches for investigating diamond wear will be discussed.

1.3.1. Conventional approaches

Optical sensor system shown in Figure 1.11 can be utilized to detect the surface morphology of working tools.[157-162] The tool wear is evaluated through comparison of the surface morphology. Due to the limitation of measuring speed, only quasi-on-line

investigation can be achieved by this type of system and the acceptance in industry is slow.[158] Cutting force has been used as an indirect indication of surface wear on machining tool.[90, 163-167] The drawback of cutting force signal method lies to the complicated conditions affecting the forces and the difficulties to develop a strong and precise system. Vibrations and acoustic emissions during machining process reveal the change on the machining tools. As a result, these signals can be employed to evaluate the wear of the tools.[168-174] Fixing sensors for detecting these signal in a suitable location is usually a problem.

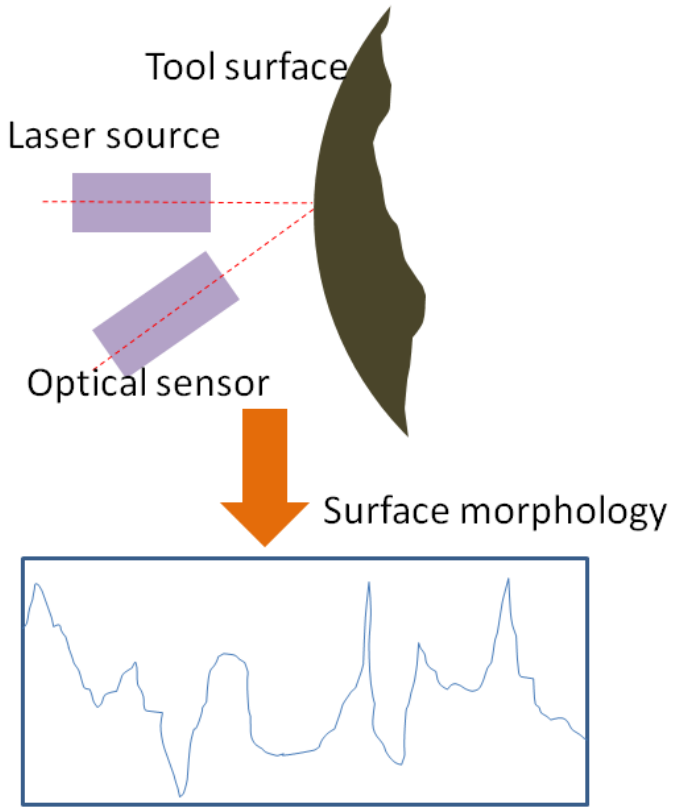

Figure 1.11. Optical sensor system for tool wear measurement.

1.3.2. Tribo-electrochemical investigation

The combination of tribological study and electrochemical investigation have been recently used to evaluate the material removal on the sample surface in chemical mechanical polishing (CMP) and electro-chemical mechanical polishing (ECMP) process.[175-179] By measuring the electrochemical impedance of the sample, the *in situ* observation in tantalum CMP and ECMP was achieved.[175] The chemical formation and mechanical removal of tantalum oxide was studied during the polishing process. The material removal process in CMP and ECMP is very similar to the material loss due to wear. In both cases, deformation of asperities or sharp peaks is generated due to external effects and materials are forced to be detached from their original site. In addition, multiple components determine the final result. Mechanical force induces the friction force between two surfaces in contact. Chemical reactions leads to change of chemical composition and surface structure. Electrochemistry positively or negatively affects these processes. From the perspective of basic reactions, the mechanism of wear and material removal in CMP and ECMP is the same. Therefore, it is possible to use the tribo-electrochemical approach to study wear of diamond containing materials.

CHAPTER II

MOTIVATION AND OBJECTIVES

Diamond is the hardest material on earth. Diamond composites have been one of the hardest material systems today. As stated in Chapter I, diamond materials are widely applied in occasions where they rub with another surface. Under external load, loss caused by friction and wear of either diamond or the other phase is one of the major concerns in applications of this type of material. Diamond materials possess excellent mechanical properties but their wear sometimes leads to serious accidents in industrial applications. Without thorough understanding of their wear mechanisms, failure prediction has not been possible. In order to improve the performance of mating pair containing diamond materials, better understanding of interfacial behavior and tribological properties of diamond is highly desired.

Due to poor industrial productivity of diamond, it is impossible for diamond bulk to be widely applied. Small particles and thin films are the two primary forms of diamond materials in current applications. Based on this background, diamond grits reinforced ceramic (Si and SiC) composites and nanocrystalline and microcrystalline diamond films are studied in the present research. These composites are chosen because silicon cemented diamond materials have shown excellent resistance for erosion wear in spray drying powder processing. The reported superior high stiffness and hardness of this type of material also make them potential applicant in heavy

machinery industry. On the other hand, the high wear resistance and outstanding biocompatibility of nanocrystalline and microcrystalline diamond enable them to be promising materials for biomedical applications. The composites will be synthesized by means of reaction sintering to form silicon carbide as the primary binder phase between the diamond particles. The thin films will be prepared using microwave plasma chemical vapor deposition (MPCVD). These materials are characterized and investigated in this study. The tribological properties and interfacial behaviors are evaluated based on the experimental results.

There are three major objectives in this research. The following chart illustrates the approaches to achieve these objectives.

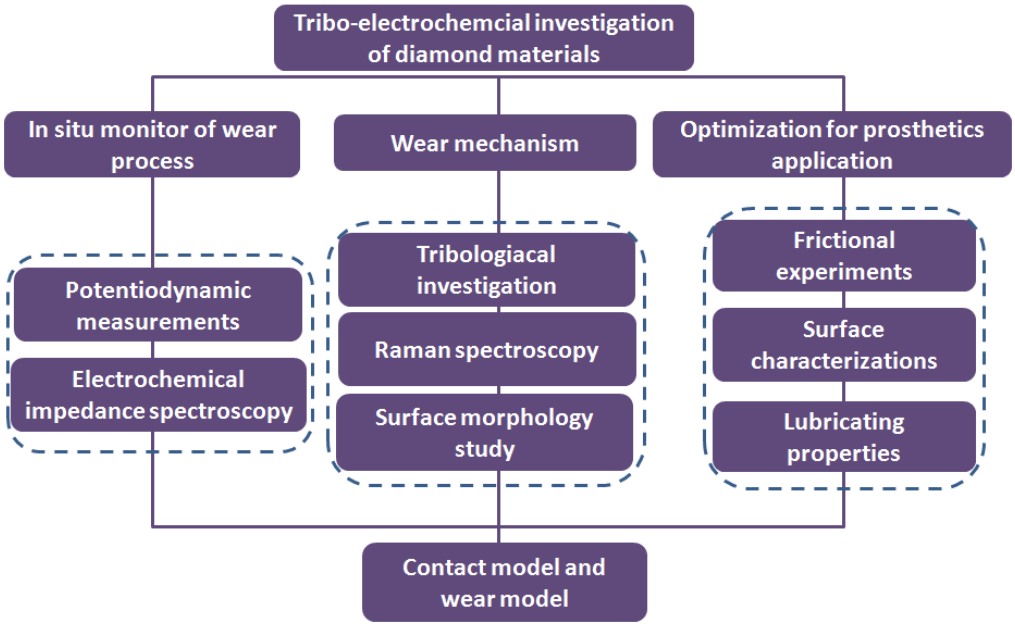

Figure 2.1. Flow chart of this research.

2.1 Development of a novel approach to monitor the friction of diamond *in situ*

Unpredictable wear of materials usually leads to disastrous consequences. *In situ* monitoring of a wear process is scientifically interesting and practically important. There is no approach available to real-timely detect the wear of insulating diamond. A novel electrochemical method will be proposed in this research to monitor the change on diamond surface.

2.2 Investigation of the mechanism of wear of diamond composites

Diamond-reinforced ceramic composites present a type of material with ultrahigh hardness and strength. These materials usually work under harsh conditions. Drilling and mining tools, for instance, have to sustain extremely high contact pressure and frequent shock. In order to improve the design and service life of these components, it is necessary to understand the wear mechanism, which has not been well studied. Tribochemical examination of the diamond composites will be conducted using a pin-on-disk configuration in both aqueous and dry environments. Characterization will be carried out on worn disks and wear debris to identify the possible processes on the diamond surface during friction and wear.

2.3 Optimization of the diamond-cartilage friction pairs

Nanocrystalline and microcrystalline diamond are potential candidates for coating film on artificial joint in biomedical applications. The tribological properties of

the diamond film will be dramatically impacted by different fictionalizations. Understanding interfacial behavior of diamond with different functionalized groups will benefit the development of prosthetics. By using tribological approach, the interfacial properties of diamond-biomaterial contact will be revealed.

CHAPTER III

MATERIALS AND METHODS

Approaches and procedures employed in the present research are described in this chapter. The first section reveals the information about the materials used. The second section description about the characterization approaches. Details on tribological experiments and electrochemical investigation are also introduced in this chapter.

3.1. Materials

Two diamond-reinforced ceramic composites (DRCC) were investigated in the current research. They are composed of silicon, silicon carbide and diamond grits. The two types of composites have the same compositions but each component shares different weight fractions. The compositions and mechanical properties of these two composites are listed in Table 2.1. The one with less amount of diamond and smaller grit size is designated as DRCC-1. The second one with more and larger diamond grits is designated as DRCC-2. The silicon carbide and silicon serve as the binder phases to hold the diamond particles together in reactive sintering. Samples were made into disks and hemispherical pins to facilitate the tribotest in a pin-on-disk configuration. The diameter and the thickness of the disk are 50.5 mm and 7 mm, respectively. The diameter of the pins is 8 mm.

In order to evaluate the tribological behavior and interfacial properties of diamond-biomaterial contact, human cartilage was selected as the mating phase with diamond surface. The human cartilage used in this study was a piece of hip joint cartilage , which was obtained from Shandong Orthopedic Hospital, China. Six diamond samples were prepared, including nanocrystalline diamond (NCD), ammonia treated NCD (NCD-NH_3), hydrogen treated NCD (NCD-H_2), microcrystalline diamond (MCD), ammonia treated MCD (MCD-NH_3), and hydrogen treated MCD (MCD-H_2). The NCD was deposited on silicon surface using MPCVD method with argon-rich $CH_4/H_2/Ar$ plasmas. The MCD was prepared by means of DC arc jet CVD in circulating $CH_4/H_2/Ar$ environment. The as-deposited MCD was then polished with diamond grinding wheels. Hydrogen treatment was carried out at 750-800 °C for 15 min while ammonia treatment was at 300 °C for the same time. More details about the sample preparation can be seen in other references.[41, 180]

3.2. Characterization

Optical microscope was used to examine the composite disk surface after frictional experiments. The surface morphology of cartilage after wear test was also investigated using the optical microscope to check the influence of long time friction on surface morphology.

Table 2.1. Composition and mechanical properties of the two diamond composites.

	DRCC-1	DRCC-2
Diamond (wt.%)	55-65%	20-35%
SiC (wt.%)	30-40%	65-75%
Si (wt.%)	2-10%	<6%
Density (g/cm^3)	3.33-3.38	2.85-3.1
Hardness (HV)	3922	2746
Young's Modulus (GPa)	760	450
Poisson's ratio	0.12	0.15

The thin diamond films were studied using Raman spectrometer (Horiba 520i, HORIBA, Ltd.) to determine the impact the functionalization on the surface structure. The surface of diamond composite DRCC-1 and its wear debris were measured as well. The wavelength of the excitation laser was 532 nm. The spectra were scanned from 400 cm^{-1} to 2000 cm^{-1}.

The composite disk surface was checked by scanning electron microscope (SEM) (Vega, Tescan Corp.) with an accelerating voltage of 15 kV after sputtering coating (PVD75, Kurt J. Lesker Corp.) of a 10 nm layer of Chromium.

Surface roughness of the diamond grit in the composite before and after frictional experiments were compared using a profilometer (DEKTAK, Veeco Instruments Inc.). 2D and 3D profile of the worn disk surface was obtained using a Keyence VK9700 profilometer (Keyence Corp.).

The surface morphology of thin diamond film was evaluated using an atomic force microscope (Nano-R2, Pacific Nanotechnology) in noncontact mode. Nanorule

(Pacific Nanotechnology, Inc.) program was employed for analysis and image processing.

3.3. Tribological investigation

In the current research, the coefficient of friction (COF) in the contact was measured using a pin-on-disk tribometer (CSM Instruments). The schematic illustration of the setup is displayed in Figure 3.1. During the experiments, weight was applied on the steel rod to generate load. The supporting arm, steel rod and the pin were fixed together and stayed still in the experiment. The disk was attached to the stage, which could be driven to move in either cyclic linear or rotational motion. The friction force and COF were recorded by the piezoelectric sensor and exported after the experiment. The applied load can be adjusted from 0.01 N to 10 N and the range of the speed is from 10 rpm to 600 rpm.

In the experiments for the composites, rotational mode was firstly used. The disk was attached to a rotating polyvinylchloride (PVC) stage and the pin was fixed to the steel rod in Figure 3.1 of the tribometer through a Teflon rod. The rotating stage has the shape of a cup and was filled with water during experiments. The distance from the pin to the center of rotating disk was 18.8 mm. In order to evaluate the impact of load and speed on friction, the applied load was increased from 2 N to 10 N and rotating speed was adjusted from 10 rpm to 30 rpm. Both the pin and the disc was immersed in water, which served as lubricant.

Due to the high wear resistance of diamond, relatively high load was necessary to generate notable wear track. Pin-on-disk experiments were carried out with two pins forced against the disk using an industrial tribotest setup. The center and the contact points of two pins on the disk were positioned in a straight line. The distance from each pin to the center of the disk was equal. This design is to increase the test efficiency of hard materials. The resulting wear track diameter on the disk was 15.24 mm. The load applied to each pin was 250 N resulting a total load of 500 N. The experiment was run for 8 h at a sliding speed of 79.4 mm/s in an aqueous environment. The accumulating sliding distance was 2,298 m.

Wear debris was necessary for the analysis of wear mechanism. In aqueous environment it was very difficult to collect the wear debris. As a result, linear mode was then applied in dry condition to generate adequate amount of wear debris. The linear motion mode was utilized in order to collect pilled-up debris at two ends of the wear track. The experiments lasted for 10 min with a load of 10 N and a maximum linear speed of 79.4 mm/s. Each measurement of COF was repeated three times for statistic analysis. After the frictional experiments, the composites surface was characterized.

In the experiments for diamond-cartilage contact, the cartilage was attached to the steel rod in Figure 3.1. The diamond sample was attached to the stage which reciprocally move with a length of 3 mm. During the frictional experiments, DI water and commercial calf bovine serum (Thermo Fisher Scientific Inc.) was added into the

contact as lubricant. The COF under different conditions was measured. The sliding speed was changed from 2 mm/s to 6 mm/s with an increment of 1 mm/s while the applied load was increased from 0.5 N to 1.5 N with an increment of 0.25 N. Relatively small loads and speeds were applied to mimic the real hip joint. Each experiment was repeated three times under the same conditions. The diamond samples were cleaned with acetone and the cartilage was cleaned with ethanol before each experiment. In order to evaluate the influence of friction on the surface morphology of cartilage, wear test was carried out with a fixed load of 1 N and a fixed sliding speed of 6 mm/s for 2000 cycles. After that, the surface of the cartilage was characterized using optical microscope.

3.4. Electrochemical study

Besides tribotests, the potentiostatic electrochemical impedance spectroscopy (EIS) and potentiodynamic experiments were utilized to evaluate the electrochemical properties at the interface of diamond-diamond contact. The EIS and potentiodynamic measurements were carried out using a Gamry potentiostat (Reference 600, Gamry). The potentiostat has three electrodes, namely working electrode, counter electrode, and reference electrode. A drop of silver paint was used to connect a conductive wire and the pin.

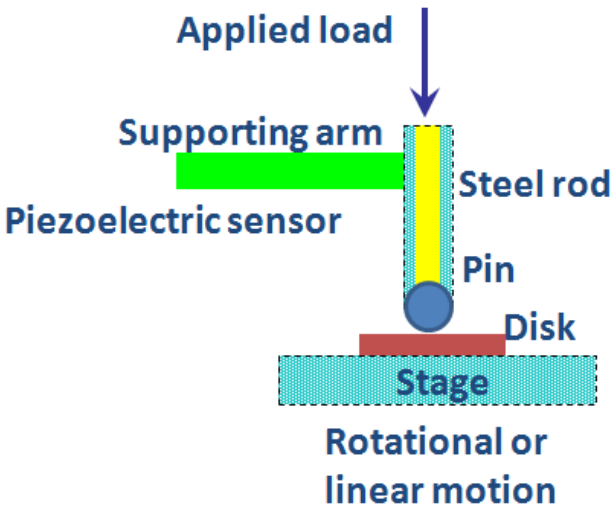

Figure 3.1. Schematic of experimental setup for tribological measurement.

As a result, the pin can serve as the working electrode in the electrochemical investigation system. The PVC stage and Teflon rod described in section 3.2 separated the composite pin and disk from other conductive components in the system. During experiments, all three electrodes were submerged in water. The expression of the experimental setup is shown in Figure 3.2. Bode plot and Nyquist plot were generated from the EIS tests. COF curves and the Tafel curves were obtained through tribotests and potentiodynamic measurements, respectively.

All experiments were performed following a specific procedure. The experiment was conducted for 5 min at a constant load and speed to allow the system to stabilize. When the system reached the steady state, the potentiostat was activated and the EIS measurement was started. As soon as the EIS measurement was completed, the potential dynamic experiments were then conducted. During the EIS

test and potential dynamic measurement, the COF was recorded simultaneously through the tribometer. After the experiment, the Bode plot and the Nyquist plot were analyzed using Gamry EIS 3000 program to obtain the equivalent circuit model. The measured Tafel curves were analyzed to investigate the impact of loads and speeds on the phase transformation and wear process.

The EIS measurements were performed by scanning frequencies from 0.05 Hz to 1 MHz with an AC potential of 100 mV. In the potentiodynamic experiments, the scanning range was -1.4 V to 0.4 V for DRCC-1 and -1 V to 1 V for DRCC-2. The scanning rate and sampling rate were 5 mV/s and 1/s (1 Hz), respectively.

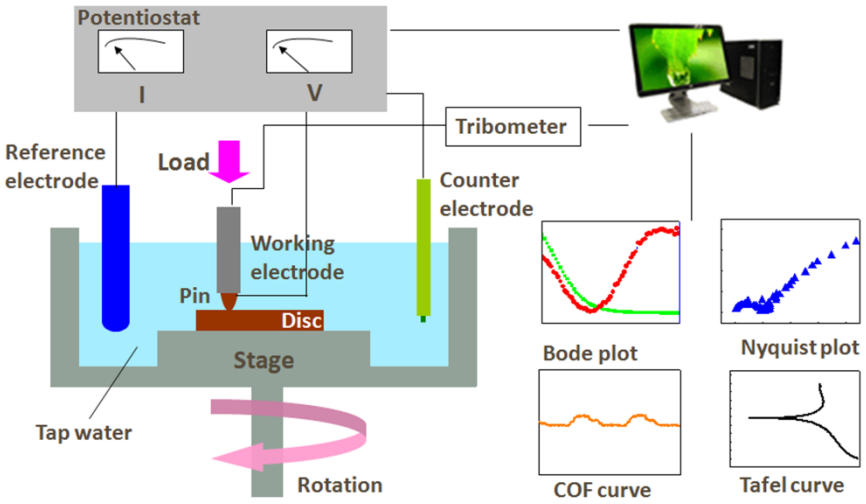

Figure 3.2. Schematic of experimental setup for electrochemical measurement.

CHAPTER IV

IN SITU MONITOR IN FRICTION AND WEAR THROUGH TRIBO-ELECTROCHEMICAL CHARACTERIZATION[1]

During rubbing, interfacial properties at the contact reveal information about friction and wear. In this chapter, an electrochemical method will be developed to monitor the wear process of two diamond-reinforced ceramic composites (DRCC). These samples have different diamond grits sizes and concentrations and the friction process takes plan in an aqueous environment. The *in situ* method to be developed includes setups for potentiodynamic measurements and electrochemical impedance spectroscopy. The tribo-electrochemical performance of the two composites will be investigated. The impact of applied load and rotating speed on COF will be evaluated.

4.1. Development of an *in situ* method to monitor the friction and wear process

In situ monitor of a wear process is scientifically interesting and practically important. Unpredictable wear and failure of mechanical components could be avoided and the stability of the whole system will be improved if *in situ* monitor is possible. We have recently developed a novel approach using tribo-electrochemical principles to study

[1]Part of this chapter is reproduced by permission of The Electrochemical Society from "In Situ Tribo- Electrochemical Evaluation of Wear of Diamond Composites" by *Huaping Xiao, et al., J. Electrochem. Soc.,* 2014, *161*, E87-E92 (Copyright © 2013, The Electrochemical Society)

material removal and degradation in chemical mechanical polishing process for metals.[175, 176, 179] In this study, a setup containing a tribometer and a potentiostat will be assembled for this purpose. The electrochemical impedance spectroscopy (EIS) and potentiodynamic measurements will be used as an analytical tool to evaluate the surface chemical conditions. The experimental setup and conditions were described in Chapter III. The results of potentiodynamic measurements will be discussed in this section.

In the potentiodynamic experiments, the change of current density passing through the composite surface with applied potential was recorded during rubbing. Physicochemical change on the surface can be evaluated based on the experimental results. Tafel curves at different conditions are illustrated in Figure 4.1. The measurements under different loads and rotating speeds are compared. The Tafel curves of DRCC-1 show little change when the applied loads or rotating speed is increased. For DRCC-2, different phenomenon is observed. The Tafel curves shift to lower potential and higher current density with increasing load and rotating speed. More interestingly, in the magnified plots the Tafel curves show wave patterns.

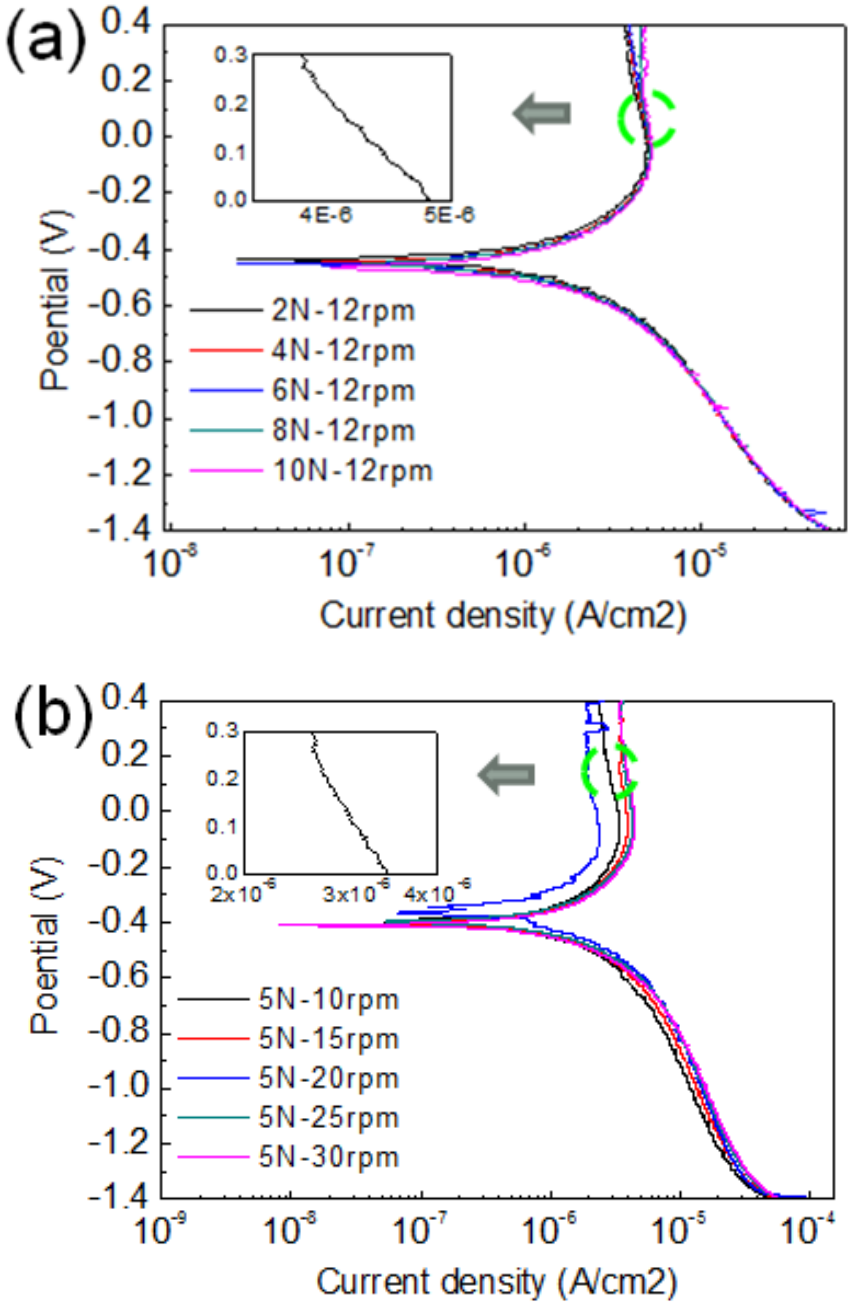

Figure 4.1. Relation between applied potential and responding current density (Tafel curve) in potentiodynamic measurements for DRCC-1 (a, b) and DRCC-2 (c, d) under different loads and rotating speeds (The inserts are magnified plots at positive potential under 2 N and 12 rpm/ 5 N and 10 rpm).

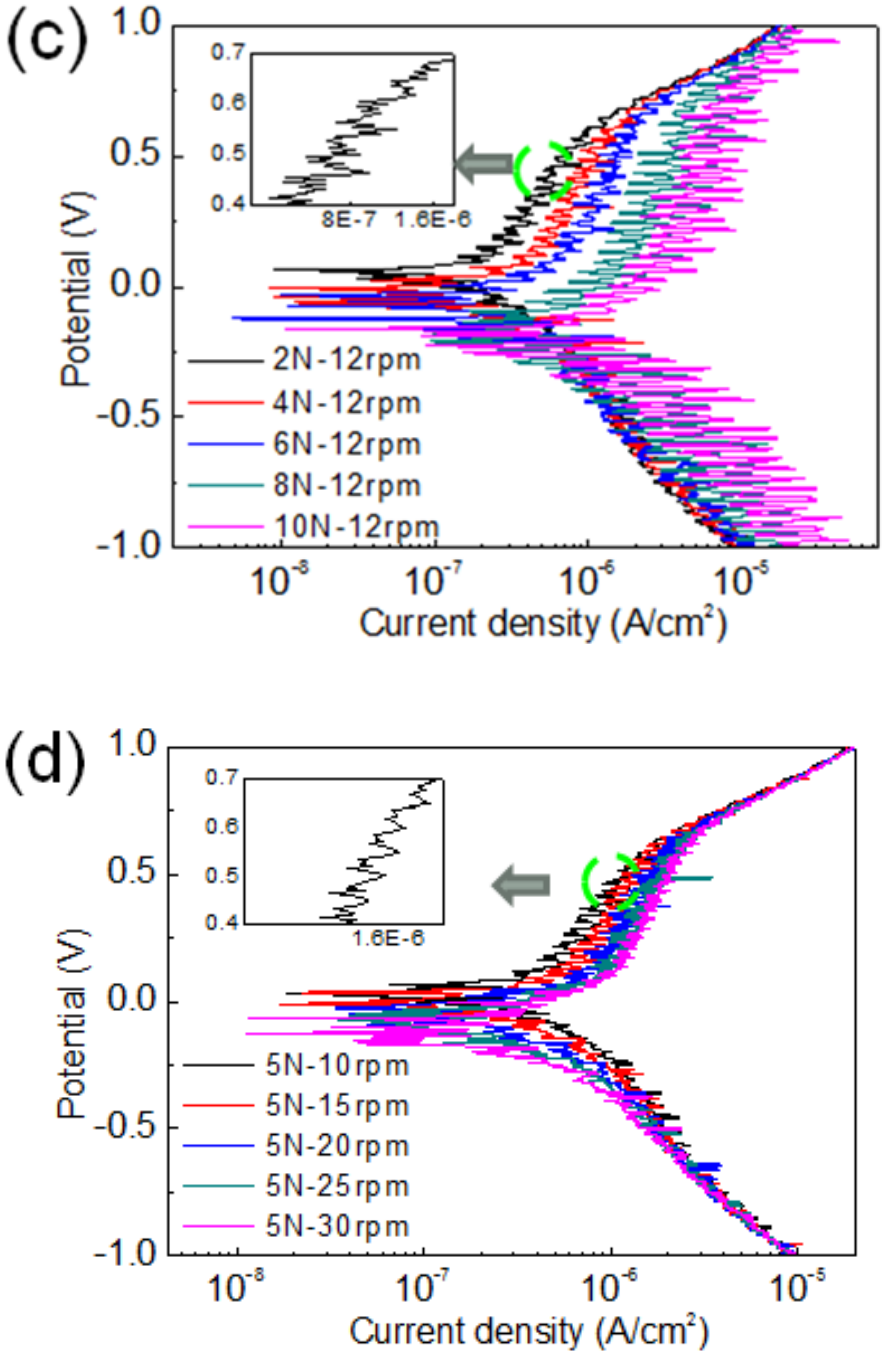

Fig. 4.1. Continued.

When the pin and disk come into contact, the diamond particles sustain the applied load because Si and SiC are easily removed. During friction, Si and SiC were worn first as illustrated in Figure 4.2. Figures 4.2 (a) and (b) reveal the 2D and 3D profile of the DRCC-1 after friction experiments, respectively. In Figure 4.2 (a), the profile along a diamond particle is displayed. It is clear that the diamond surface is higher than the surrounding phase. The plateau region indicating the diamond particle and valley region showing the ceramic phase can be identified in Figure 4.2 (b). The relatively elevated diamond particle confirms that the ceramic phase was removed before the diamond particles. The two surfaces in contact are diamond-diamond in most occasions. Due to the non-uniform distribution of diamond particles the applied load could be sustained by only a few diamond particles. This leads to small real contact area, resulting high contact pressure. The phase transformation from sp^3 bonded carbon (diamond) to sp^2 bonded carbon(amorphous carbon) occurs under high pressure in the tribotest.[181-183] In this study, the transformed amorphous carbon is removed by harder diamond particles on the counter face during tribotests. The electrical conductivity of amorphous carbon is much higher than that of diamond.[184, 185] Therefore, the phase transformation from diamond to amorphous carbon and the wear of the amorphous carbon can be evaluated by the change of electrical properties. In the potentiodynamic measurement, such amorphization-wear process is demonstrated by the periodic change of the current density. When the diamond surface is amorphorized, the conductivity increases and so does the current density. The conductivity and the

current density decrease as the amorphous carbons is removed.

Figure 4.3 shows the measured, fitted and calculated relation between potential and current density of DRCC-2 under 5 N and 15 rpm. To facilitate the calculation, the x axis and y axis of Tafel curve were interchanged. Current density is exponentially related to potential according to Tafel equation.[186] That is:

$$i = mV^n \quad (4\text{-}1)$$

where i is the current density, V is the potential, m and n are constants to be determined from curve-fitting of the measured data. In this study, the amorphization-wear process produced sinusoidal pattern. So Equation 4-1 is modified to:

$$i = mV^n + a\sin(\frac{2\pi}{T}V + \theta) \quad (4\text{-}2)$$

where a is the amplitude of the sine function, T is the period and θ is the shift of the phase. The value of m and n were obtained by means of non-linear curve fitting using the Origin 8 program. The fitting curve is displayed in Figure 4.3. Substituting the value of m and n into Equation 4-2, a, T and θ can be determined. We calculated the duration in time by evaluating the potential span in each period. Take Figure 4.3 as an example, the potential period in the figure is 27.3 mv. The scanning rate for the potentiodynamic measurement was 5 mV/s, indicating that 5 mV in potential scale stands for 1 s in time scale. As a result, the time span is 27.3/5=5.46 s.

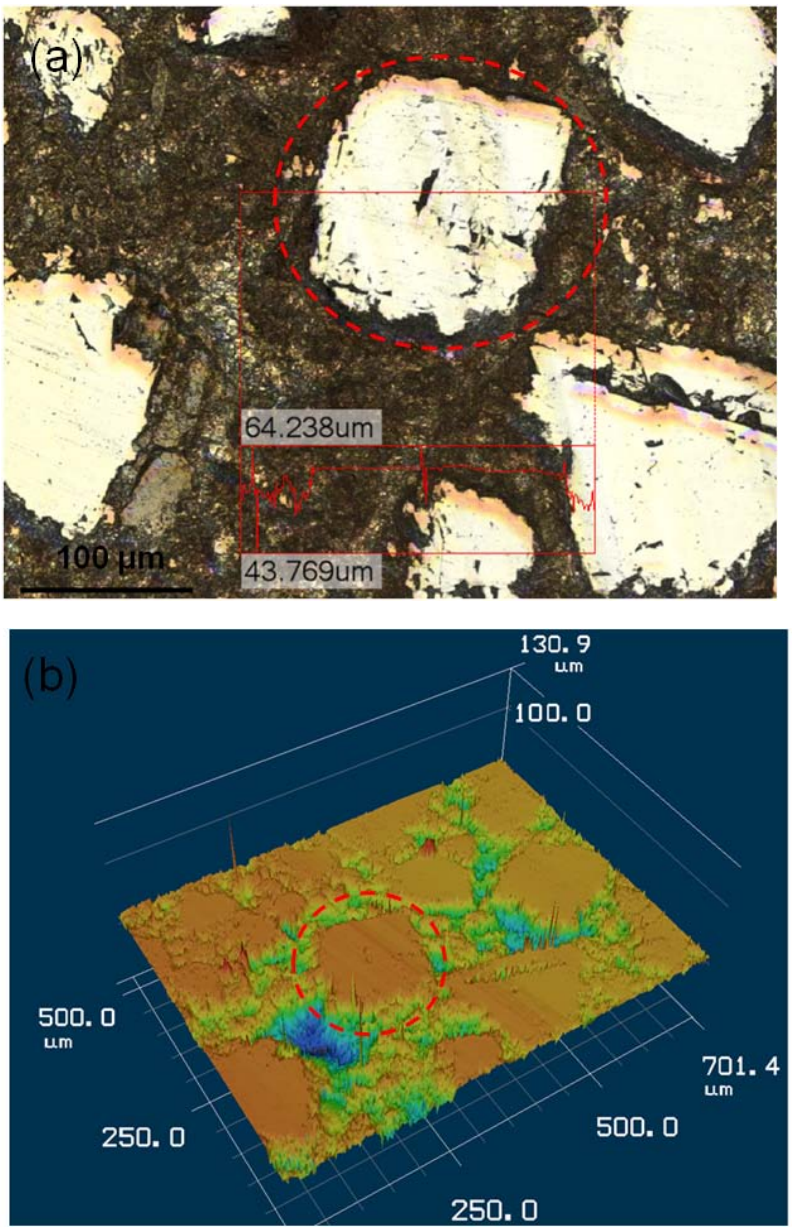

Figure 4.2. 2D (a) and 3D (b) profile of DRCC-1 surface after friction experiments, the two circles in (a) and (b) indicate the same area.

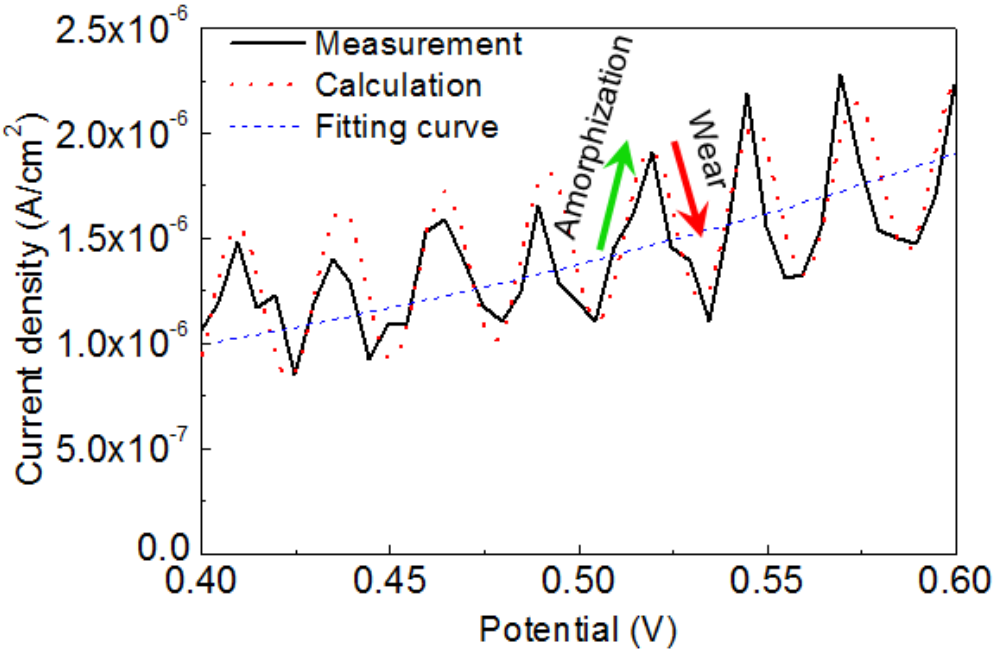

Figure 4.3. Measured (solid line), fitted (dashed line) and calculated (dotted line) relation between applied potential and responding current density of DRCC-2 under 5 N and 15 rpm.

4.2. Evaluation of frictional behavior

In this section, frictional behavior at the interface will be evaluated using electrochemical method and tribological method.

4.2.1. Electrochemical method

The impacts of loads and rotating speeds on the fluctuation behavior were analyzed by means of mathematical calculation. Table 4.1 lists the calculated values of a and T under different conditions. Similar tendencies of the calculated results are

observed for both DRCC-1 and DRCC-2. At constant rotating speed, the period of the sine function change little with loads. The amplitude, however, gradually increases as the loads is increased. When the applied load is kept constant, the period reduces and the amplitude remains stable with increasing rotating speed. More loads lead to higher contact pressure and more diamond carbon is amorphorized. More phase transformation alters electrical properties of the surface so the measured current density shows greater change. When the rotating speed is increased, the period of amorphization-wear process becomes shorter which means the amorphous carbon on the surface is removed faster. It is interesting that the calculated amplitude of DRCC-2 is much greater than that of DRCC-1. This means that more materials on the DRCC-2 surface is removed under the same condition.

Table 4.1. Calculated value of a and T under different conditions.

	2N-12rpm	4N-12rpm	6N-12rpm	8N-12rpm	10N-12pm	5N-10rpm	5N-15rpm	5N-20rpm	5N-25rpm	5N-30rpm
DRCC-1										
a	0.12	0.22	0.36	0.42	0.61	0.41	0.37	0.38	0.31	0.39
T (s)	8.66	7.86	7.62	7.9	7.96	9.66	5.71	3.78	2.84	2.28
DRCC-2										
a	2.8	3.6	4.4	30.2	55.1	3.4	3.8	4.3	4.8	5.2
T(s)	7.61	7.48	7.64	7.59	7.52	9.89	5.46	3.75	2.85	2.25

4.2.2. Tribological study

The frictional behavior of the composites investigated using a pin-on-disk

configuration will be discussed in this section. The change of COF with loads and speeds was recorded. Figure 4.4 (a) displays the sample curve demonstrating COF changes with time. The average value of the COF curve was estimated and used as the effective COF for each test. The test was repeated for three times. The error bars in Figure 4.4 (b) and (c) show the highest and lowest data points. The impact of the rotating speed (Figure 4.4 (b))and applied load (Figure 4.4 (c)) on COF is shown. At a constant load of 5 N, the COF of DRCC-2 decreases with increasing rotating speed whereas the COF of DRCC-1 remains stable within the same speed range (10 rpm to 30 rpm). When the rotating speed is fixed, the COFs of both DRCC-1 and DRCC-2 show an upward trend as the applied load is increased. It is clear that the COF of DRCC-1 is much lower than that of DRCC-2 under the same conditions. Considering the similar composition of the two composite, one possible reason for the significant difference in COF is due to the difference in grain size of diamond particles. As illustrated in Figure 4.2, diamond surfaces rub against each other in most occasions. The smaller particle size and lower diamond concentration of DRCC-2 lead to smaller asperity area. After the friction experiment, the area fraction (the ratio of area of diamond asperities to that of the whole surface) on the pin was measured using image processing technique. The color of the diamond grit is different from that of the ceramic phase as shown in Figure 4.2 (a). By defining a threshold value of grey level, the diamond region was easily differentiated from the ceramic phase.

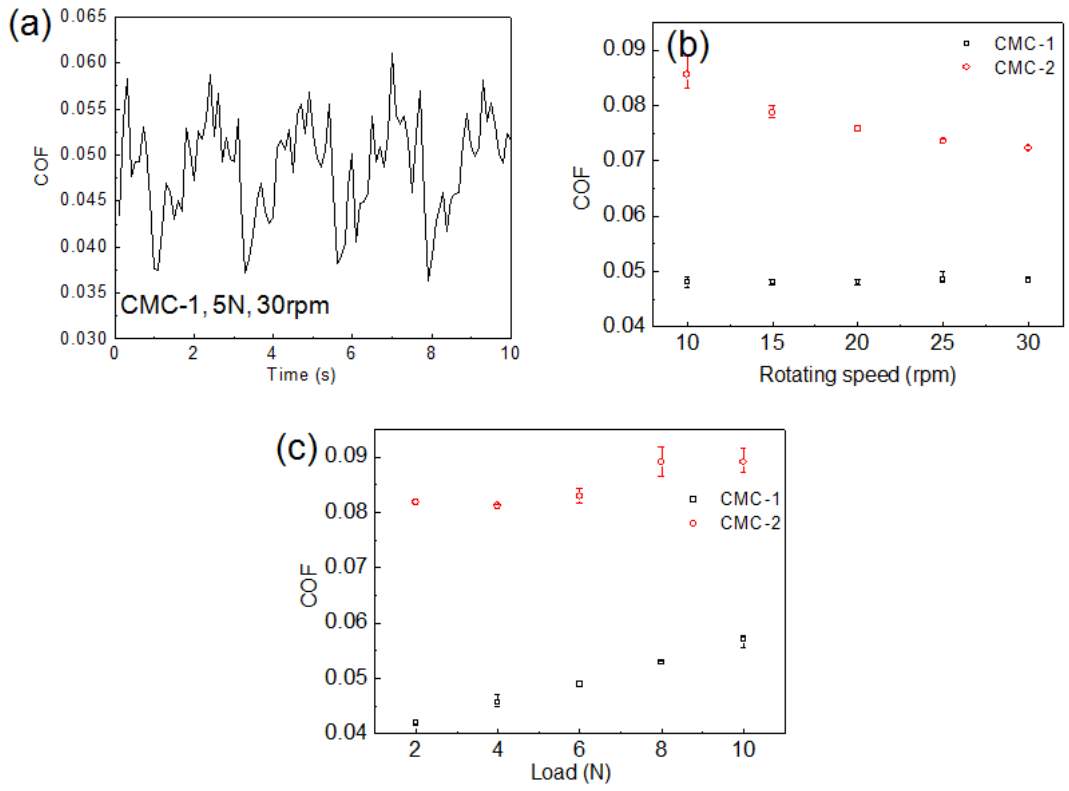

Figure 4.4. Sample curve demonstrating COF as a function of time (a), variation of COF with rotating speed (b, applied load is 5 N) and applied load (c, rotating speed is 12 rpm).

The area fraction of DRCC-1 and DRCC-2 are ~60% and ~30%, respectively. The smaller asperity area leads to higher local pressure. High pressure impedes the relative motion and further causes the increase in friction force as well as the COF. The contact pressure increases with applied load, so in both cases the COF goes up when load is raised. This result correlates with the increased amplitude of the sinusoidal pattern with rising load, which is shown in Table 4.1. The amplitude is a reliable indicator of the

friction force when the direct measurement of force is not available.

4.3. Model of the interfacial interactions

In the previous sections, a novel electrochemical method using potential dynamic measurements was developed to monitor the dynamic change on composite surface. The frictional behavior of diamond composite sliding against itself was evaluated. In this section, EIS measurements will be utilized to investigate electrochemical impedance properties on the composite surface.

4.3.1. Interfacial properties of DRCC-1in aqueous environment

DRCC-1 and DRCC-2 have the same chemical composition but the concentration of each components, namely diamond grit, Si and SiC, is different. Electrochemical properties of DRCC-1 will be analyzed in this section.

4.3.1.1. Bode plot and Nyquist plot

The change of electrochemical impedance with applied AC frequency reveals the properties of surface and interface during sliding. Figures 4.5 (a) and 4.5 (b) show relation between impedance and frequency under 5 N and 20 rpm for DRCC-1. In the Bode plot (Figure 4.5 (a)) for DRCC-1, one relaxation at 2 Hz (dotted arrow) is observed.

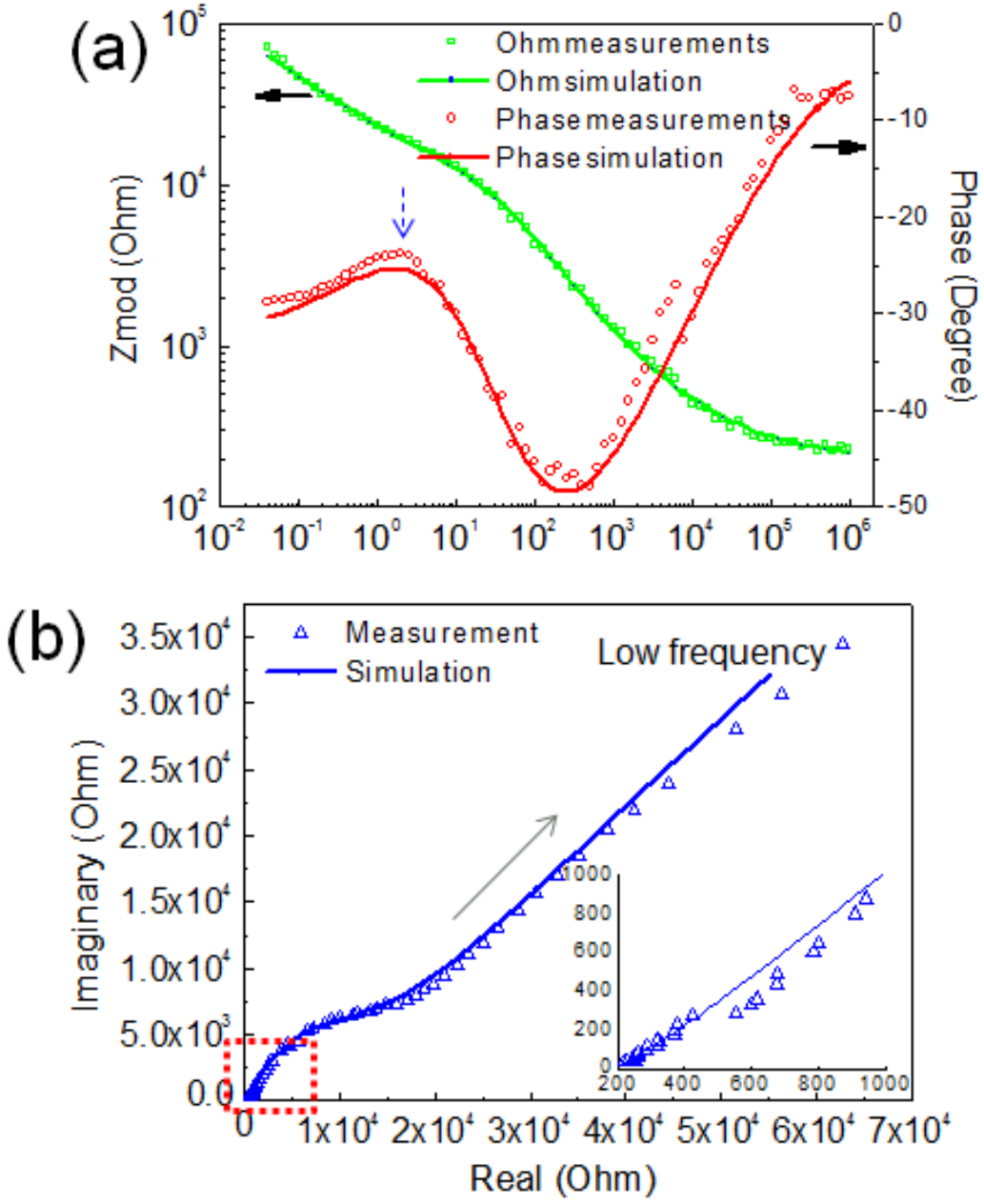

Figure 4.5. Bode plot (a), Nyquist plot (b), equivalent circuit model (c) and schematic representation (d) for DRCC-1 under 5 N and 20 rpm (Dots are measured results and curves are simulations. The insert in Nyquist plot is the magnified plot at high frequency. The arrow in Nyquist plot indicates the direction of lower frequency.).

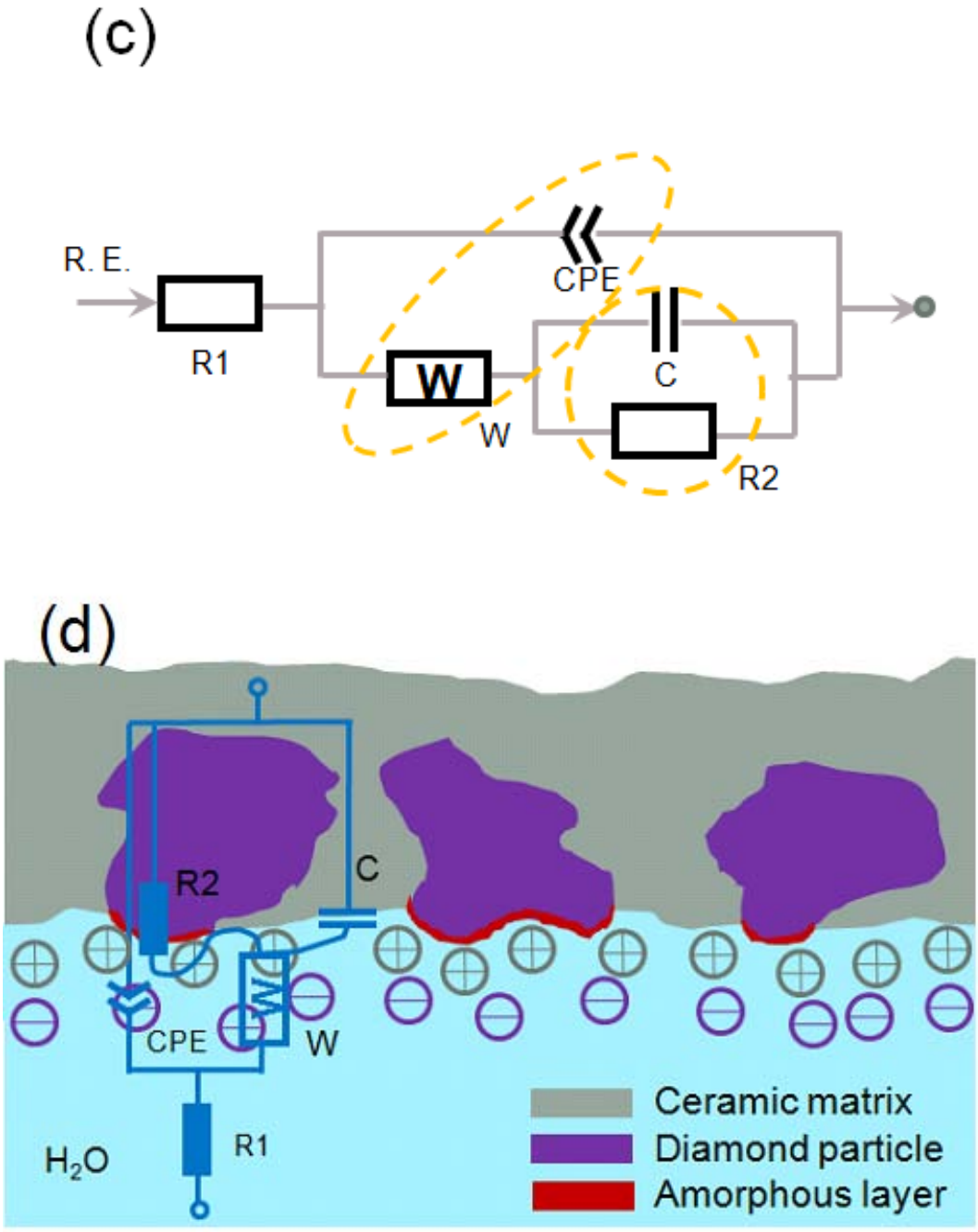

Figure 4.5. Continued.

The relaxation phenomenon is the temporary delay of the current which is induced by the change of the dielectric properties of the interface. In the Bode plot, the peak of phase angle as we can see in Figure 4.5 (a) is an indication of relaxation. The Nyquist plot (Figure 4.5 (b)) reveals the relationship between the real and the imaginary parts of the impedance at different frequencies during friction. The result of EIS experiment reflects the change of current passing through the electrode and solution with applied voltage. In most cases, the system is not pure resistive and a phase shift is usually observed due to the capacitive and the inductive component. The variation of the dielectric properties of the interface causes the change of the responding current. Therefore, the properties of the interface can be evaluated if the electrical measurements are available.

4.3.1.2. Equivalent circuit model

The equivalent circuit model (Randle model) is a widely used tool to investigate the physicochemical processed at the interface in electrode-electrolytic systems.[187] In the model the solution is usually represented as a resistor (R1).[188] In aqueous environment, an interfacial double layer is formed and two electrical components can be used to represent it.[189, 190] In the case of DRCC-1, a constant phase element (CPE) and a Warburg impedance (W) are determined by means of modeling. The relaxation phenomenon observed in Figure 4.5 (a) indicates charge transfer or formation of new components at the interface.[191] In the current system, the surface of

DRCC-1 represents a new set of electrical components. Modeling was attempted to determine the unknown components. A simple resistor-capacitor combination was generated. The complete equivalent circuit for DRCC-1 is displayed in Figure 4.5 (c). Comparison between the measured results and the simulated results can be seen in Figure 4.5 (a) and (b). Validity of the proposed equivalent circuit model is confirmed by the close match. Figure 4.5 (d) illustrates the physical model of the interface. In Figure 4.5 (d) impedance of bulk liquid is represented as R1. No chemical reaction is involved in the water so that the R1 is an ohmic resistor. Due to the excess charge on the electrode surface, ions with opposite charges in water are attracted to the interface and form the interfacial double layer. A parallel CPE and Warburg impedance combination (CPE and W) are used to describe the interfacial double layer. The imperfect capacitor (CPE) produces a phase delay less than 90°. According to the simulation result, the DRCC-1 surface is described as a combination of resistor and capacitor. The boron-doped diamond is more conductive so the diamond phase is supposed to be the resistor and the ceramic phase is represented by the capacitor. In the case of diamond, the charge transfer caused by chemical reaction is negligible due to the chemical inertia of diamond. Therefore, the resistor representing diamond is also ohmic.

4.3.2. Interfacial properties of DRCC-2 in aqueous environment

This section will focus on DRCC-2. Compared to DRCC-1, DRCC-2 has lower

diamond grit size and weight fraction. DRCC-2 presented higher friction as shown in section 5.1. The electrochemical properties of DRCC-2 with static potential will be investigated in the following.

4.3.2.1. Bode plot and Nyquist plot

The change of impedance with frequency under 5 N and 20 rpm for DRCC-2 is shown in Figure 4.6 (a) and 4.6 (b). The relaxation phenomenon (indicated by the dotted arrow) is observed at 0.35 MHz.

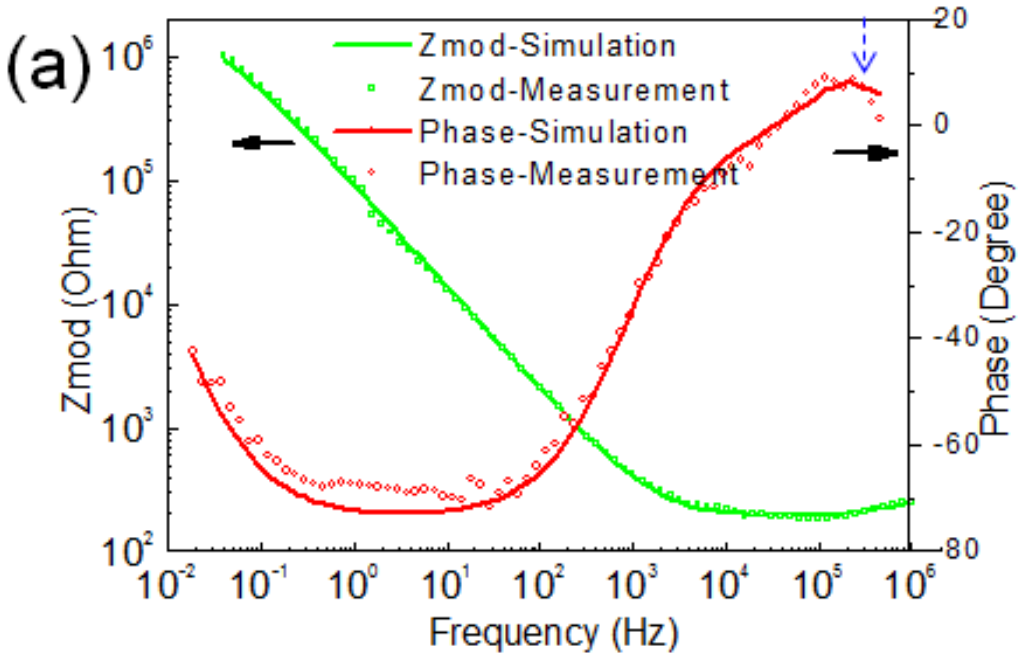

Figure 4.6. Bode plot (a), Nyquist plot (b), equivalent circuit model (c) and schematic representation (d) for DRCC-2 under 5 N and 20 rpm (Dots are measured results and curves are simulations. The insert in Nyquist plot is the magnified plot at high frequency. The arrow in Nyquist plot indicates the direction of lower frequency.).

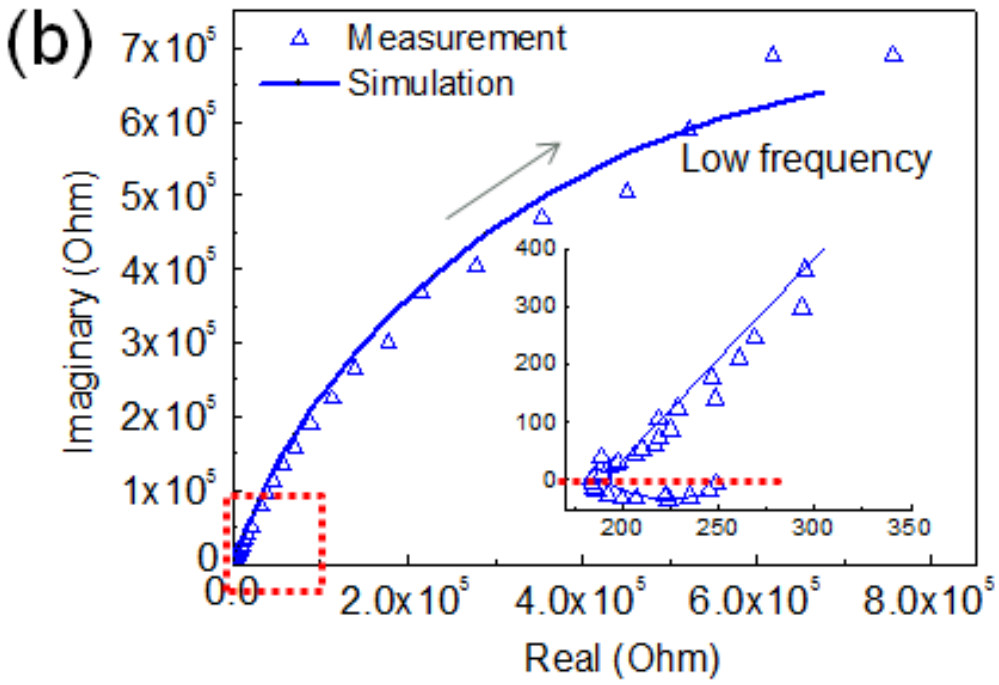

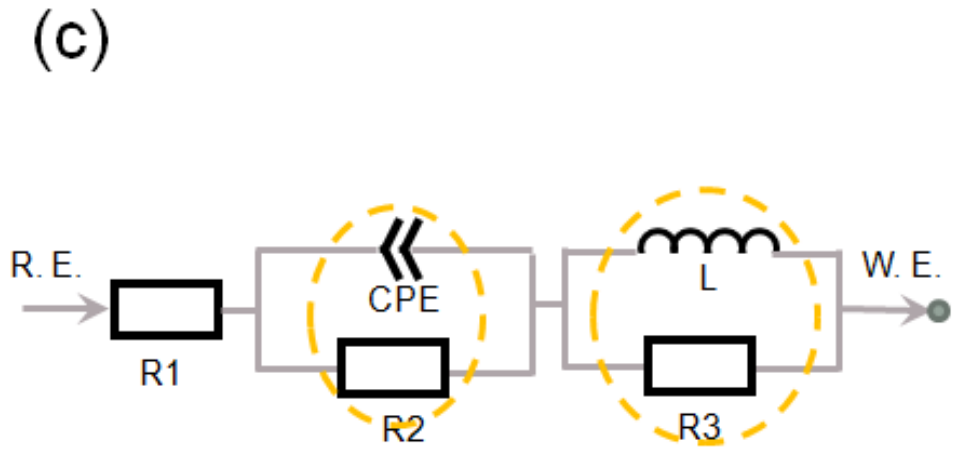

Figure 4.6. Continued.

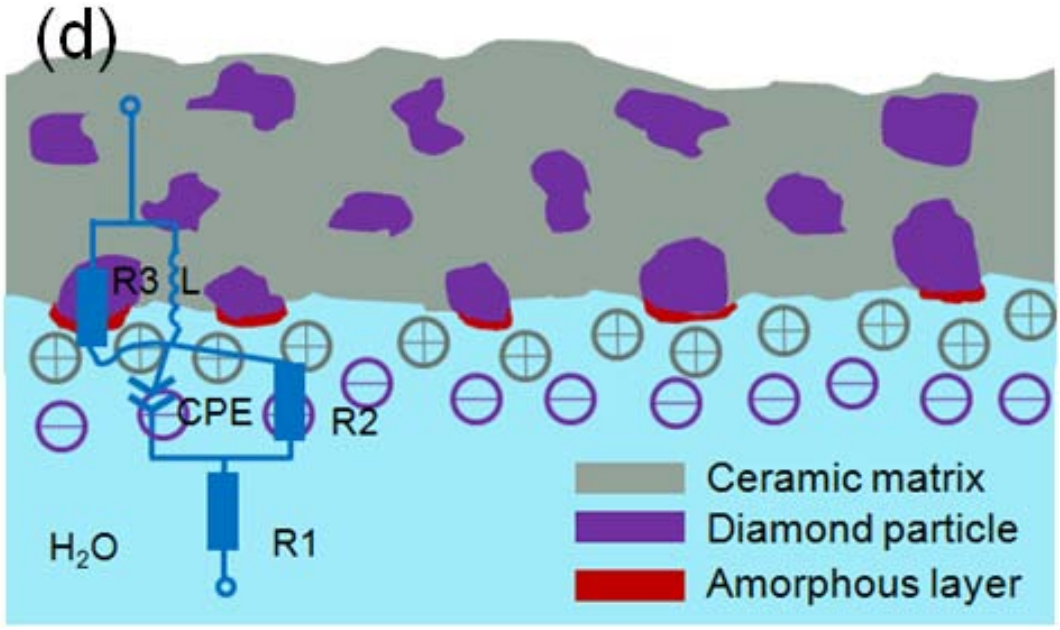

Figure 4.6. Continued.

4.3.2.2. Equivalent circuit model

In addition to the electrical components of the solution (R1) and the double layer (CPE and R2), a set of inductor and resistor were included in the model to represent DRCC-2. The proposed physical model is shown in Figure 4.6 (d). Interfacial double layer also forms at the interface in case of DRCC-2 and is represented as a paired CPE and resistor.

All the resistor are regarded as ohmic for the same reason mentioned in the discussion for DRCC-1. In DRCC-2, the density of conductive diamond particles is much less than DRCC-1.The passage for electrons in DRCC-2 is more complicated and coil-like pass ways may form. This is one explanation for the inductive component

in the circuit. The inductor causes the phase advance shown in Figure 4.6 (a). Grit size is one possible explanation for the difference between the two models. The path of electron flux inside the composite changes when a sample with a different grit size is used.

4.4. Summary

Two diamond-reinforced-ceramic composites, namely DRC-1 and DRC-2 were investigated using a tribological and electrochemical approach. A tribo-electrochemical approach was utilized to real-timely evaluate the friction and wear process on the composite surface. Even though these two composites have the same chemical composition, very different equivalent circuit models were developed based on the EIS measurements. This difference was due to the lower concentration and grit size in DRCC-2, which led to a more complicated path for electrons inside the composite. In the potentiodynamic investigation, experimental data revealed the sinusoidal behavior of the current density against potential. It was correlated to the amorphization-wear process during rubbing. The amplitude in the sinusoidal pattern is an indication of the intensity of the amorphization-wear process. This behavior was affected by the grit size of diamonds. The larger diamond grit generated less current due to lower wear in comparison with otherwise. These results show that friction and wear of the diamond reinforced ceramic phase composites can be *in situ* monitored by means of the proposed electrochemical approach. More importantly, this approach is also applicable

to monitor friction and wear process of other nonconductive material, which has not been possible until this study. Real-time detection of wear between a rubbing pair is of critical significance for the performance and safety of industrial systems. The findings in this study provide a new method to solve this problem.

CHAPTER V

MECHANISMS OF WEAR AND PHASE TRANSFORMATION[2]

In this chapter, the wear mechanisms of diamond-reinforced ceramic composite (DRCC) will be investigated. Characterization techniques utilized include Raman spectroscopy, optical microscope, and scanning electron microscope (SEM). Analysis was conducted before and after tribotests. Wear mechanisms will be proposed based on the observed phase transformation of diamond carbon in the friction process.

5.1. Characterization of wear track

During friction and wear, the surface microstructure of the composite subjects to change. In this section, the change of structure will be evaluated. Experimental conditions have been discussed in Chapter III. The optical image of the scanned region on the DC-1 disk surface is displayed in Figure 5.1 (a). Two distinct regions, the non-wear region and the wear region, can be differentiated. The non-wear region is generally dark while notable bright particles can be seen in the wear region. To understand this further, we conducted Ramon spectroscopic analysis of worn diamond samples. The reference area (no wear) was labeled as area (1) in the optical image in Figure 5.1 (a). The worn diamond particles, showed shinny spots in the same optical

[2]Part of this chapter is reproduced with permission from "Silicon-oxide-assisted wear of a diamond-containing composite" by Huaping Xiao, et al., *Journal of Applied Physics,* **2013**, *114*, 223505 (Copyright © 2013, AIP Publishing LLC)

image, were labeled as (2) to (6) in Figure 5.1 (a). Raman spectra are illustrated in Figure 5.1 (b). At spot 1, the strong peak for Si (520 cm^{-1}) and visible peaks for SiC (795 and 970 cm^{-1}) were detected. In the wear region, the intensity of the featured peaks for Si and SiC were greatly reduced. At spots 2, 3, and 4, small peaks for Si (520 cm^{-1}) and SiC (795 cm^{-1}) can be seen. At spots 5 and 6, however, no peaks for Si and SiC can be determined. With regard to the peaks for carbon, strong Raman peak for diamond around 1333 cm^{-1} were detected at all those six spots. Smooth and broad band appear near 1406 cm^{-1} (the D band) and its intensity increases as the wear of the diamond particle increases. Table 5.1 lists the intensities of the carbon peaks at different spots. Another observation is that the featured line for D band was found to shift from spot 2 to spot 6 as shown in Figure 5.1. From spot 2 to spot 6, the position of D band shifts to higher wavenumber and then shifts back. For better understanding the shift of D band, the spectra between 1250 and 1550 cm^{-1} were deconvoluted using Lorentzian fitting. Results in Figure 5.2 show that the fitted middle peak is very close to the position of the original D band.

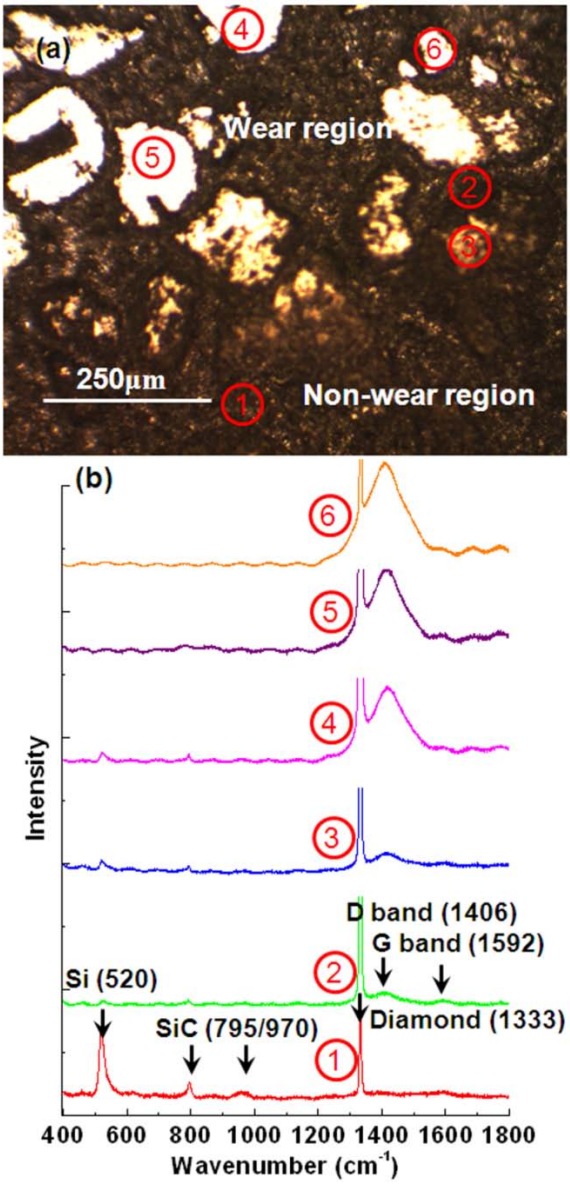

Figure 5.1. (a) Optical image and (b) Raman spectrum for DC-1 disk surface (spot 1 is in non-wear region and the other spots are in wear region, the numbers on line 3 to line 6 are the positions of D band for spot 3 to spot 6).

It is noted that for adequate comparison, the whole peaks are not shown. The position of the fitted middle peak shows an upward-downward tendency as observed in

the original spectra. In addition to the middle peak, another peak around 1460 cm^{-1} is identified by means of convolution. This peak is from the finite-size crystals of graphite.[192] Again, the according wavenumber of the right peak increases first and then decreases.

Table 5.1. Intensity of Raman peaks for carbon on DRCC-1 disk.

No. of spot	Diamond (sp^3)	D band (sp^2)	sp^3/sp^2
1	1515	30	50.5
2	11945	204	58.6
3	17865	358	49.9
4	56142	1452	38.7
5	42872	1639	26.2
6	39909	15602	2.6

The SEM images of both the non-wear (reference) region (Figure 5.3 (a) and (c)) and the wear region (Figure 5.3 (b) and (d)) were obtained. The diamond particles can be clearly distinguished in both regions. The significant difference between the two regions is that the particle surface in the wear region is smoother than that in the reference.

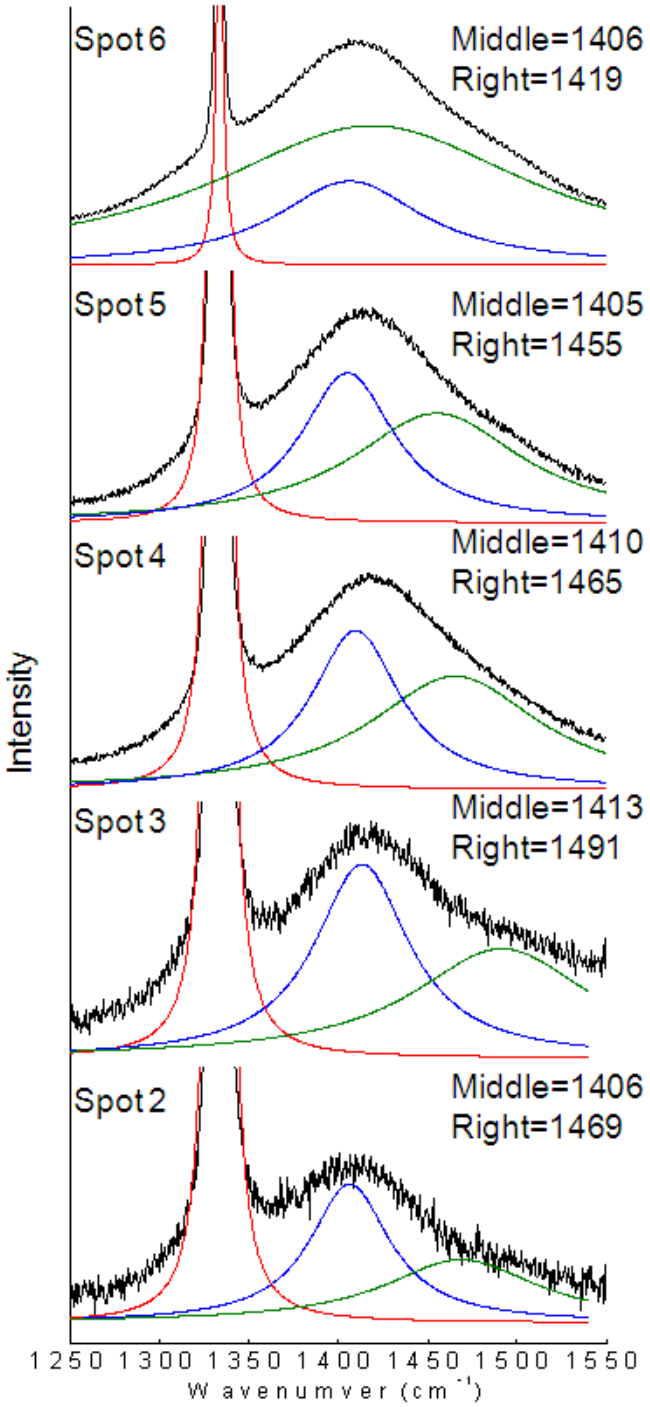

Figure 5.2. Deconvolution of Raman spectra in the range between 1250 and 1550 cm^{-1} (the positions of the middle and the right peak for each spot are shown in numbers).

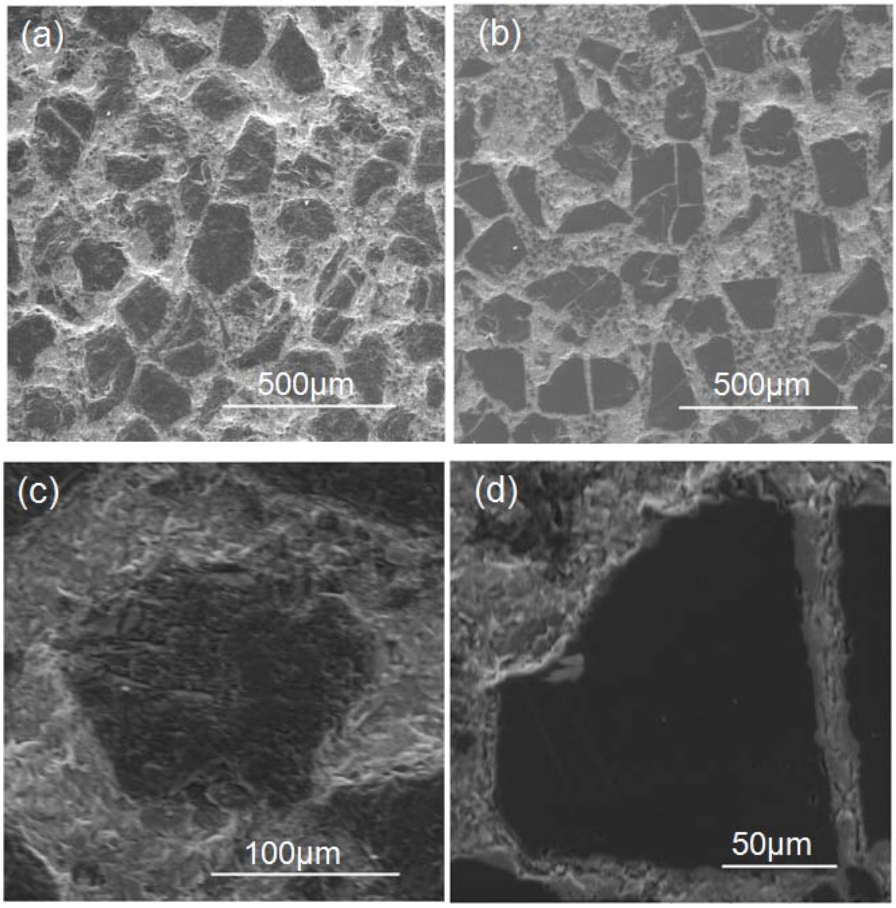

Figure 5.3. SEM images of non-wear region (a and c) and wear region (b and d) on the disk. It is clear that the diamond was polished.

The measured surface roughness of the diamond particles in the wear region is 33.9±12.8 nm. In the non-wear region, the exact value of roughness cannot be determined because it was out of the measuring range. It is clear that it is more than 1 μm. According to Figure 5.3, it is obviously seen that the diamond grits are polished. This is correlates with the shiny surfaces observed under the optical microscope in the wear region (Figure 5.1 (a)).

5.2. Characterization of wear debris

In order to achieve compressive understanding of the structure change in wear process, the study of wear debris is necessary. The Raman spectra of wear debris are shown in Figure 5.4. The blue (top) and green (middle) lines are for the wear debris and the red line (bottom) is reference. There is a sharp peak detected at 510 cm^{-1} for debris 1. Based on previous studies,[193, 194] the crystalline Si has a characteristic peak at 520 cm^{-1}. When being oxidized, this peak shifts toward lower wavenumber down to 480 cm^{-1}, where a mixture of amorphous Si and silicon oxide existed. With amorphization, these peaks are widen.[195] According to those, it is clear that the peak at 510 cm^{-1} is believed to be a sign of oxidized Si due to friction.

Compared to the reference plot, the featured peaks for C in wear debris shifted from 1333 cm^{-1} to 1326 cm^{-1} in debris 2. Zhao et al.[196] observed similar downshift of Raman peak when diamond particle size was reduced. This is correlated with the shift of the Raman peak. A high intensity band at 1596 cm^{-1} was detected. This is a typical G band (sp^2 bond) confirming the existence of sp^2 bond in the wear debris. It is important to note that in Figure 5.1, according to the Raman pattern the debris 1 is most likely obtained from SiC/Si phase and the debris 2 from diamond grits.

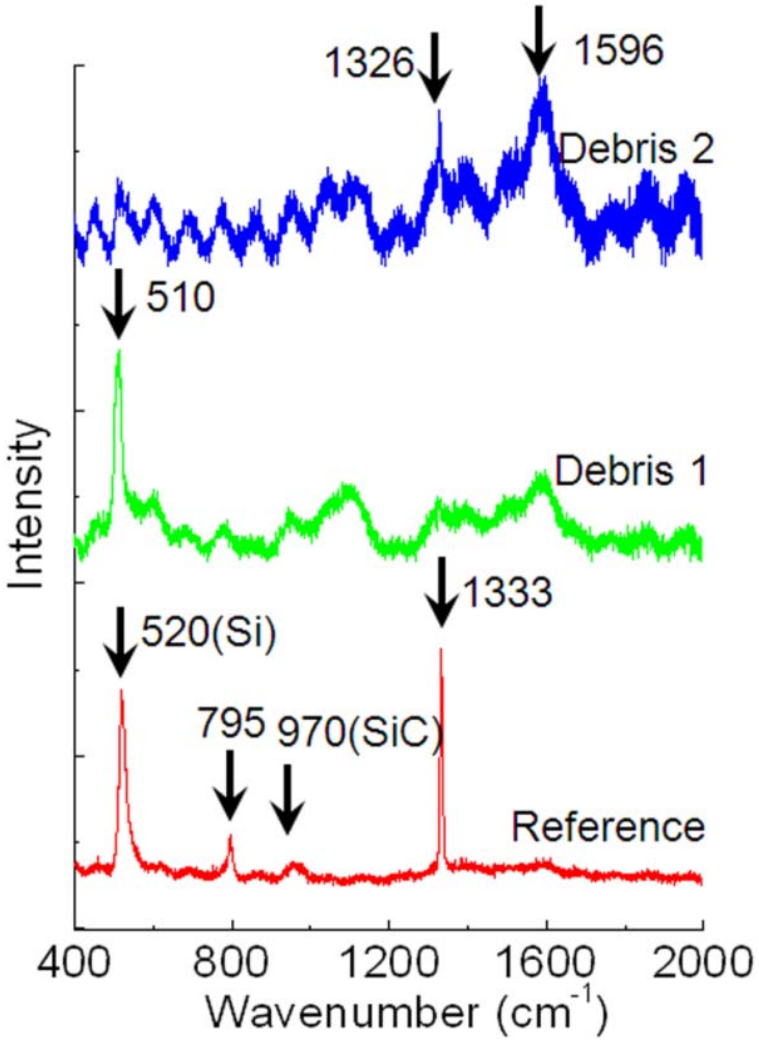

Figure 5.4. Raman spectra of wear debris and non-wear surface.

5.3. Phase transformation from diamond carbon to amorphous carbon

The physical properties of the carbon-based composite strongly depend on the chemical bonding (diamond sp^3 bond and disorder/graphite sp^2 bond) that interlink the carbon atoms.[197, 198] The Raman peak around 1333 cm^{-1} is an indicator of cubic

diamond of pure sp^3 bonds.[199, 200] As a matter of fact, except for the peak at 1180 cm^{-1}, all other lines detected by Raman in the range of 1000-1650 cm^{-1} are considered to originate from carbon with sp^2 bonds.[201] The most important two features for sp^2 bonds are the D and G band. The broad D band ranges from 1280 to 1400cm^{-1} and G band ranges from 1520 to 1600 cm^{-1}. [202, 203]

In the case of DC-1, the decreasing ratio of diamond peak to D band and the broadening of the D band demonstrate the change of sp^3 into sp^2 bonds. The phase transformation from diamond carbon to amorphous carbon (a-C) took place as evident by the decreasing sp^3/sp^2 ratio. With high sp^3 bonds concentration (above 80%), the a-C is recognized as tetrahedral carbon (ta-C) in order to distinguish it from ordinary sp^2 a-C with lower sp^3 concentration. On the disk surface the coexistence of cubic diamond, ta-C, and a-C is possible because of the nonuniformity of hardness and pressure distribution in friction process. At spot 1, 2 and 3, no shiny diamond particles are observed, indicating there is no severe wear at those spots. The sp^3/sp^2 ratio is high and cubic diamond is the dominating component at those 3 spots. The wear at spots 4, 5 and 6 is visually more intense compared to spots 2 and 3 as observed in Figure 5.1 (a). The results of Raman spectra showed that the intensity ratio of sp^3/sp^2reduces when more wear is generated on the diamond particle. This means the concentration of ta-C and a-C increases and sp^3 bonded carbon transfers to sp^2 bonded carbon with the wear process. In this study, the experiments were done in aqueous environment so the thermal effect in the phase transformation is negligible. Pressure and shear stress are

the two major contributors for the sp^3 to sp^2 conversion.[182, 204, 205] According to Pastewka et al.,[182] at the amorphous carbon-diamond interface, the carbon atoms cannot move so the shear stress is close to zero. The origination of bond breakage is from pressure and shear stress only works inside amorphous carbon.

Regarding the Raman peak shift, the shift of the D band could be attributed to two possible reasons. The first explanation is the change of the molecular structure of carbon. Any change of the molecular structure could induce the variation of the vibrational state of the carbon. In the friction process, the chemical bond between the carbon atoms could change and defects could be generated due to the wear of the interface. Stress is another possible reason for the shift of D band. High contact pressure was applied to the surface during the friction test and it is highly possible that residual stress remains in the structure. The downshift of D band under strain had been observed in graphite oxide and carbon fibers.[206, 207]

5.4. Wear mechanisms of diamond-reinforced composite

In this study, the wear experiments were conducted in both aqueous and dry environment. In aqueous condition, the heat generated due to friction dissipated quickly through water. The observed phase transformation is not the consequence of the rise in temperature. Under the applied load of 250 N the local contact pressure could be up to 31.8 GPa. Under such stress, the phase transformation from sp^3 bonded carbon to sp^2 bonded carbon is induced. This is correlated with our previous study in

diamond-like carbon.[195] Furthermore, crystalline Si was found to be amorphized and oxidized due to sliding. It is well known that amorphous silica is a polishing agent.[196,208] It is interesting that in our diamond-containing composite, the oxidized silicon produces a polishing agent that actually promotes wear of diamond. In this case, the weak sp^2 bonded carbon is prone to be removed.

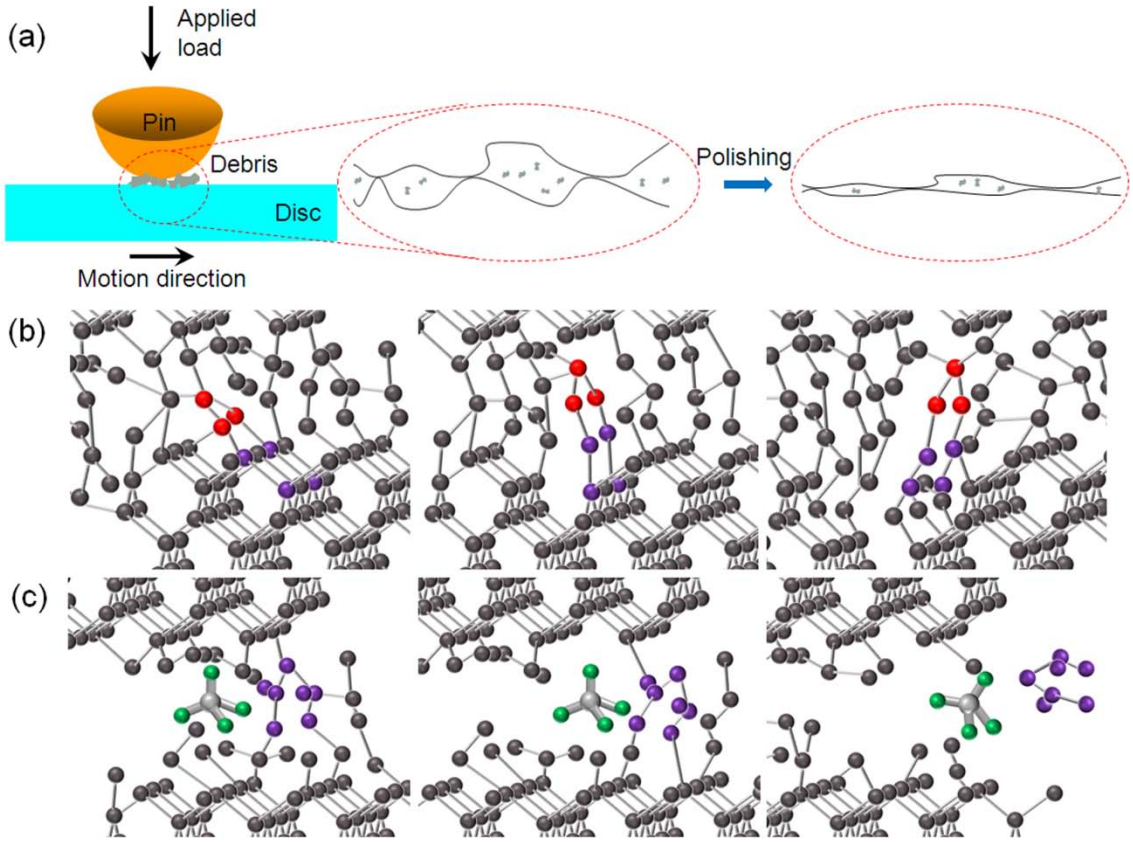

Figure 5.5. (a) Schematic expression of wear model of diamond composite in friction process, (b) The amorphization process for diamond carbon (the carbon atoms in different layers are displayed in red (sp^2) and purple (sp^3)), (c) The silicon oxide assisted wear of sp^2 carbon.

This mechanism is illustrated in Figure 5.5. In dry condition, the wear process is similar to that in wet condition due to humidity (R.H. ~40%) except that the temperature is higher because the generated heat accumulates at the contact. High temperature could promote the phase transformation and dislocation generation. These changes took place even though a smaller applied load.

5.5. Summary

This chapter discussed the wear mechanism of diamond grits reinforced ceramic composite. In this study, the ceramic phase was a combination of silicon and silicon carbide. The specific type of composite presented a class of materials with ultrahigh hardness, stiffness and strength. The worn disk surface and wear debris after tribological experiments were characterized using Raman spectrometer, SEM, and profilometer. Comparison of Raman spectra on the disk showed that the intensity ratio of sp^3 bonded carbon to sp^2 bonded carbon decreases as the wear of diamond particle increases. The phase transformation of diamond carbon to ta-C, a-C and graphite like carbon is confirmed by the decrease of sp^3/sp^2 ratio. The SEM images showed that the surface became smoother after the tribological experiments. The smoothing was confirmed by the reduced roughness of the diamond grits from above 1 μm to 33.9 nm.

The Raman peak of wear debris identified a shift from crystalline Si (521 cm^{-1}) to the mixture of amorphous silicon and silicon oxide at 510 cm^{-1}. This meant that Si transformed from crystalline to both amorphous and oxidized structures. The phase

transformation weakens the mechanical strength of carbon at the interface. The formation of amorphous silica particles as polishing agent promoted wear rather, polishing, of diamond that was evident under SEM observation. This was also confirmed by the smoothening and reduction of the surface roughness of diamond particles. The discovery and understanding of wear mechanism in the present study was also applicable to other types of diamond reinforced composite. Diamond had much higher hardness than other materials so other phases in the composite were removed first as discussed in Chapter IV. High contact pressure between diamond-diamond contact led to phase transformation. After that the weaker amorphous carbon was removed. In this research, SiO_2 served as polishing agent. For other diamond reinforced composite there could be no such smoothing effect.

CHAPTER VI

DIAMOND-CARTILAGE FRICTION-PAIR FOR POTENTIAL APPLICATIONS IN PROSTHETICS

This chapter will explore the potential applications of diamond materials in prosthetics. As a promising material for biomedical applications, diamond has attracted great attention due to its chemical inertness, low friction, and excellent biocompatibility. Tribological performance of the cartilage-diamond contact in deionized water and calf bovine serum environments will be investigated for fundamental understanding. To optimize lubrication, hydrogen and ammonia treatment will be applied on diamond surfaces. Adhesion and wettability on different diamond surfaces will be studied to determine the impact of functionalization on surface properties.

6.1. Investigation of surface morphology with and without functionalization

Surface morphology of the two mating surface is directly related to friction. In this study, the same cartilage will slide on different diamond surfaces. In order to evaluate the impact of functionalization methods on surface morphology, AFM was used to scan the diamond surface and results are displayed in Figure 6.1. It is obvious that the grain size for NCD series is between 10 nm to 30 nm and that of MCD is about 1-2 μm. No obvious change of morphology is observed after functionalization.

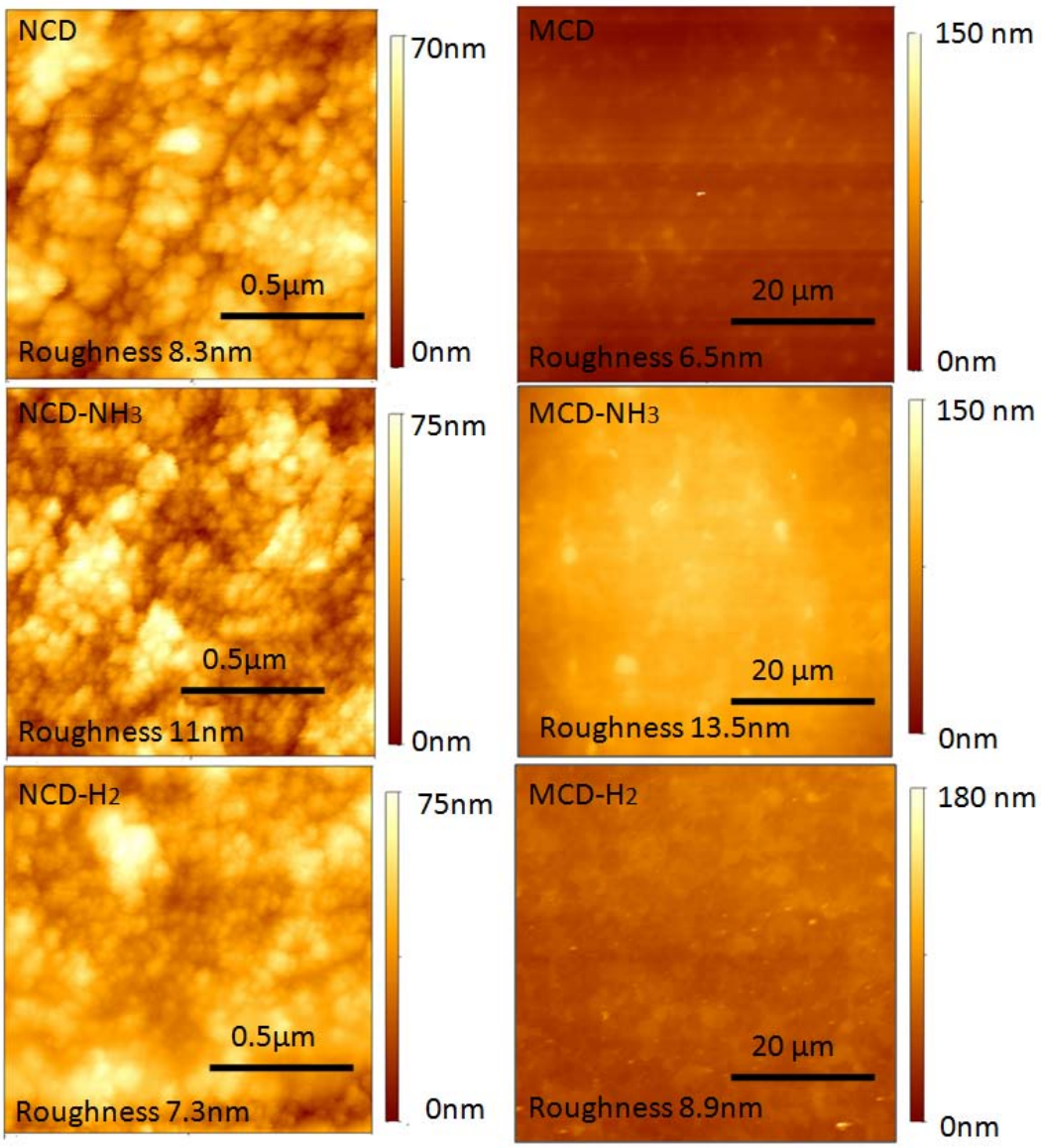

Figure 6.1. AFM images showing surface morphology of NCD series (left column) and MCD series (right column), the first row is as-deposited samples, second row is after ammonia treatment, and the third row is after hydrogen treatment.

6.2. Surface microstructure characterized using Raman spectrum

Raman spectra of the six diamond samples, which were obtained under the same conditions (wavelength of excitation laser is 532 nm with a power of 0.3 watt), are displayed in Figure 6.1. For the NCD series, there is no sharp peak observed for carbon bond. Three broad bands at 1136 cm^{-1}, 1333 cm^{-1}, and 1587 cm^{-1} are seen. They are typical bands for NCD.[19, 209-211] The D (1333 cm^{-1}) and G (1587 cm^{-1}) bands are related to sp^2 bond and can be detected in Raman spectrum due to the grain boundary in NCD structure.[19] There is no obvious change of the spectra for NCD after ammonia and hydrogen treatments. For the three MCD samples, sharp peak at 1333 cm^{-1} indicating cubic diamond is observed. The diamond peak is due to the sp^3 bond between carbon atoms. In addition to the sharp peak, the D band is also detected. After treatment with hydrogen, the band for sp^2 bond shifts to 1130 cm^{-1} and 1586 cm^{-1}. Its position changes to 1226 cm^{-1} after ammonia treatment. The band shift is due to the interaction between the dangling bond on the surface and the -H or $-NH_2$ end group from hydrogen and ammonia treatment.

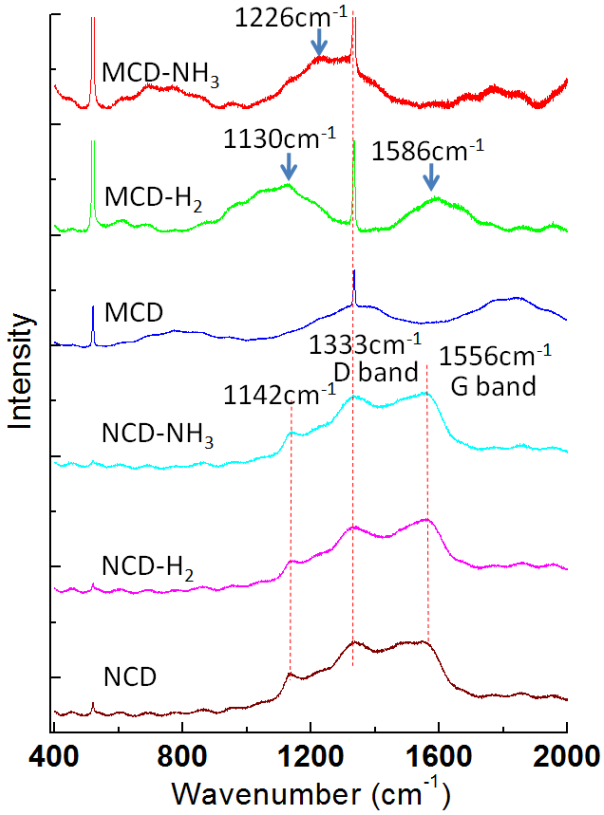

Figure 6.2. Raman spectra for diamond.

6.3. Impact of functionalization on contact angle and adhesion force

Contact angle of DI water on different diamond surfaces are compared in Figure 6.3. For pure NCD and MCD, the measured contact angles are 82° and 56°, respectively. The contact angles decrease to 54° and 42° after ammonia treatment. Being treated in the hydrogen environment, the diamond surfaces become more hydrophobic. The contact angles increase to 86° and 92° as shown in the last row of Figure 6.3. The sp^2 bonded carbon has lower surface energy than that with sp^3 bond. When the other conditions are the same, the contact angle on MCD surface is lower

than that on NCD. The change of hydrophobic properties after functionalization was attributed to the adsorption phenomenon on the surface of diamond.[212-214]

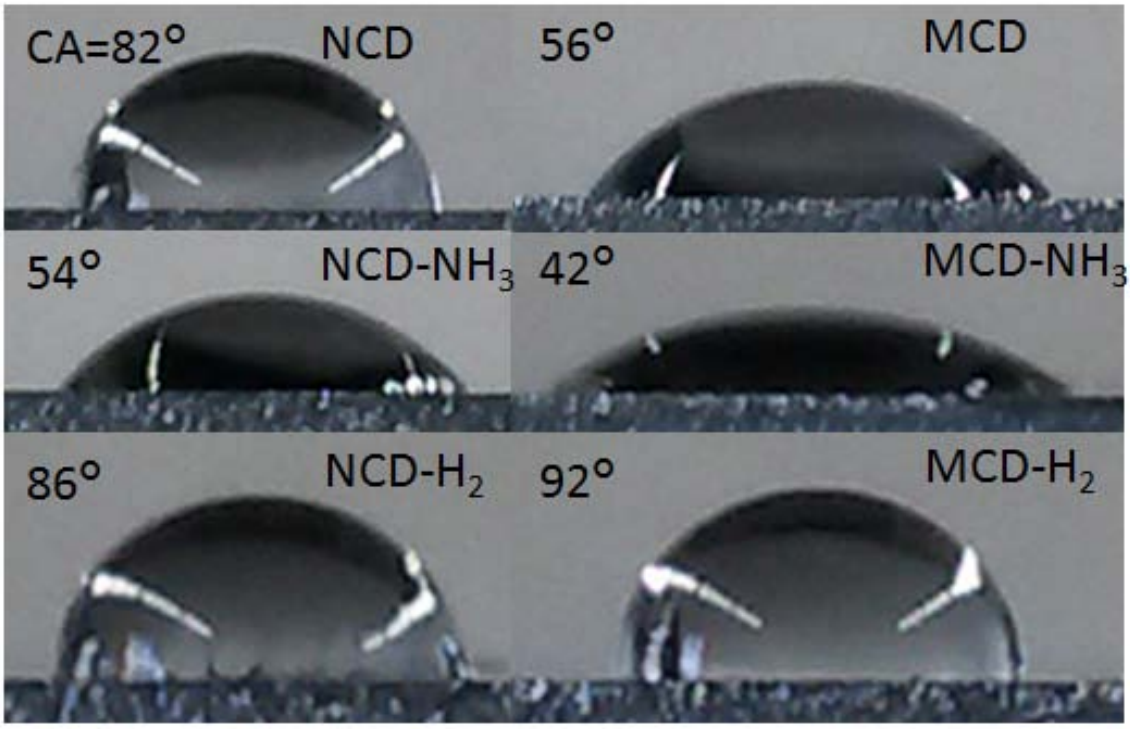

Figure 6.3. Contact angles of DI water on different diamond surfaces.

In order to confirm the impact of functionalization on surface adhesion, the displacement-output voltage curve was obtained using the AFM. A typical curve is illustrated in Figure 6.4. The AFM tip utilized in this study is a typical contact mode tip. It is made of Si_3N_4 with a radius of 40 nm and a spring constant of 0.2 N/m. The sample stage was moved up until it reached a preprogrammed height. Then it was retracted to the original position. In the retracting process, the detachment of AFM tip

and sample surface produced a sudden increase of output voltage as displayed in Figure 6.4. The displacement of the AFM tip at the detachment point can be quantitatively evaluated. Given the spring constant of the cantilever, the adhesion force can be calculated.

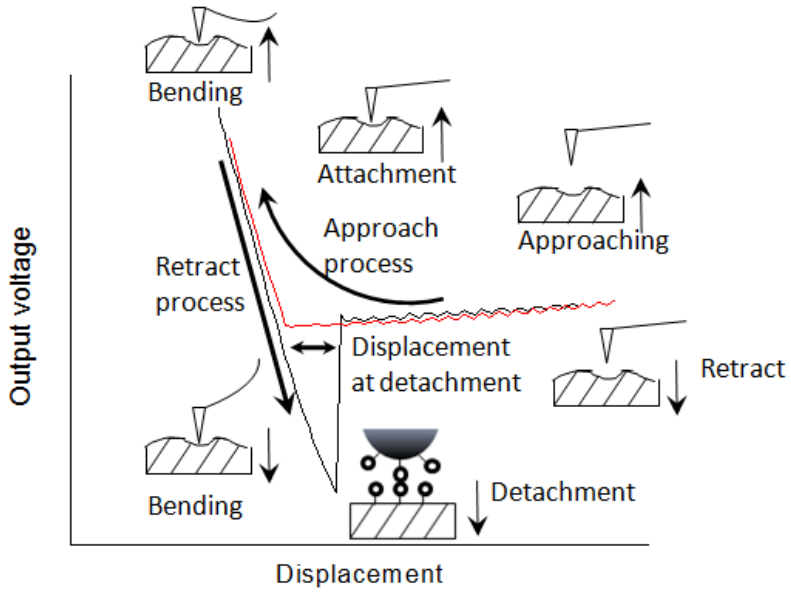

Figure 6.4. Schematic of typical displacement-output voltage curve for adhesion force measurement (the distance indicated by the double sided arrow is the displacement of the AFM tip at the point of detachment).

The displacement-output voltage curves on different sample surfaces were obtained and illustrated in Figure 6.5 (a) and (c). The calculated adhesion force based on the curves in Figure 6.5 is shown in Figure 6.6. In Figure 6.6 (a), the displacement of the AFM cantilever at the detachment point is 95 nN. This value decreases to 14 nN

after hydrogen treatment. Ammonia treatment, on the other hand, increases the adhesion force on the microcrystalline diamond to 162 nN. Similar effects of the fictionalization on adhesion force are found on microcrystalline diamond surface. The calculated adhesion forces on MCD, MCD-H_2, and MCD-NH_3, are 736 nN, 531 nN and 785 nN, respectively. During the hydrogen treatment, chemisorption of hydrogen saturated dangling bonds by forming C-H bonds on the surface. After the saturation, the reduced adhesion force (Figure 6.5) indicated the lowered surface energy. Such decrease in the surface energy was believed to induce hydrophobicity (Figure 6.3). On the contrary, the ammonia treatment increased surface energy , leading to the increase of hydrophilicity (Figure 6.3).

There are two possible explanations for this phenomenon. The nitrogen atoms were doped into the substrate, producing N-C polar bonds. These bonds are more attractive to water molecules than the nonpolar C-C or C=C bonds. As a result, more hydrogen bonds are established between diamond surface and water molecules and contact angle decreases. On the other hand, NH_2 end group can be terminated onto the diamond surface by saturating the dangling bonds, leading to increase of surface energy and decrease of contact angle.

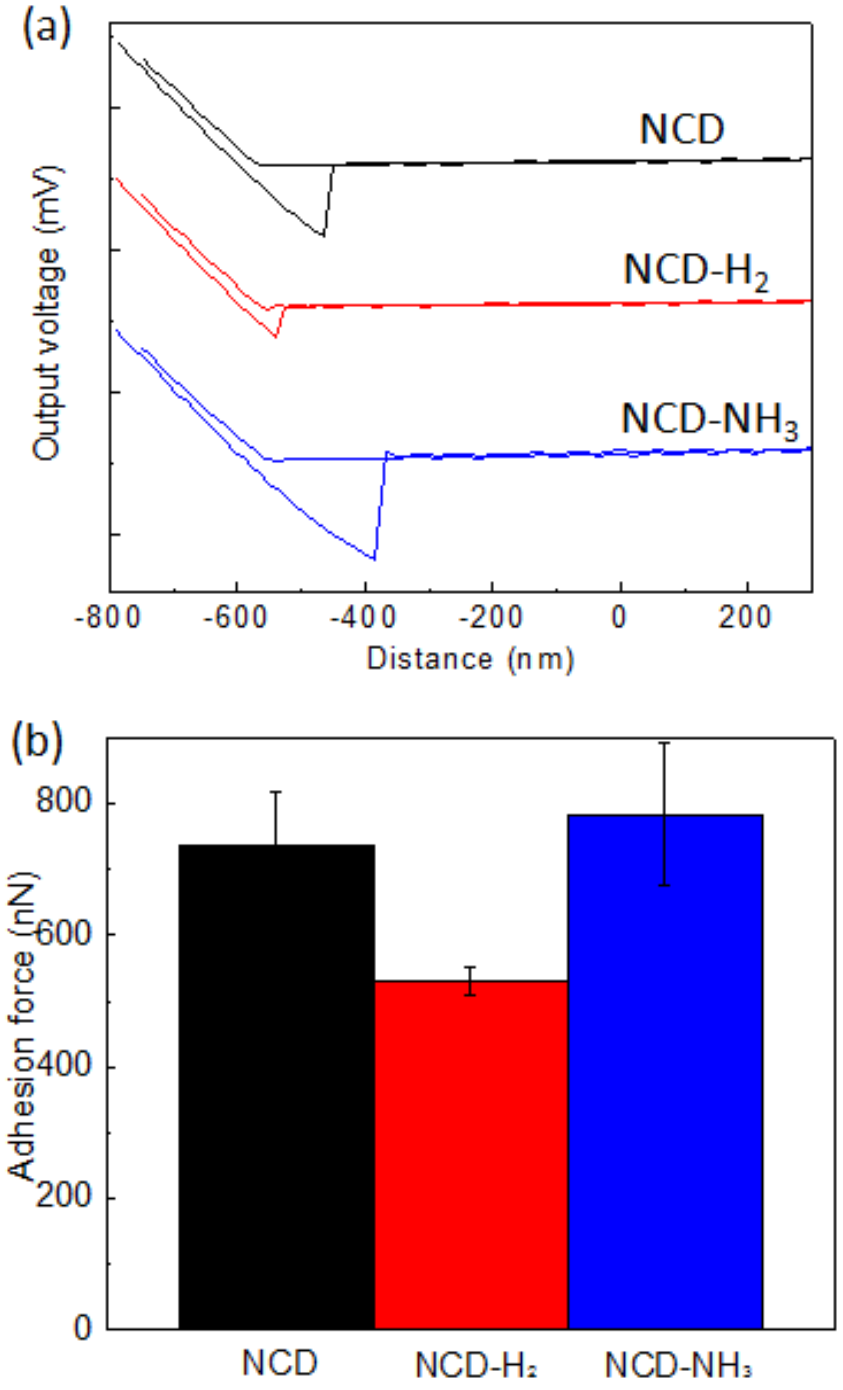

Figure 6.5. Displacement-output voltage curves (a, c) and calculated adhesion force (b, d) for nanocrystalline and microcrystalline diamond with and without fictionalization.

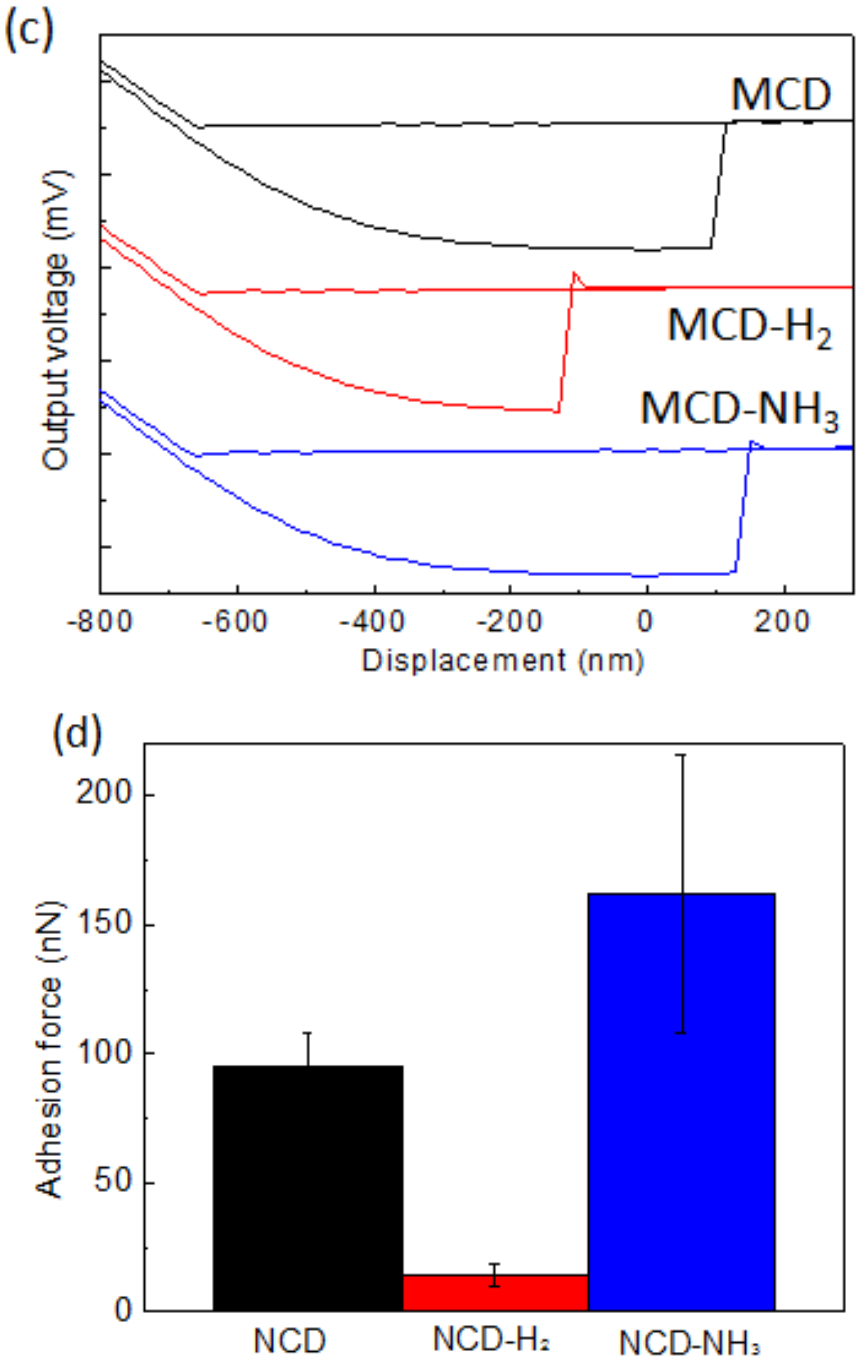

Figure 6.5. Continued.

6.4. Tribological performance under lubrication

To investigate the impacts of applied load on friction, the COF was measured at different loads while the sliding speed was fixed at 2.5 mm/s. The results are compared in Figure 6.6. Figure 6.6 (a) and (b) illustrates the measurements when DI water and calf bovine serum were used as lubricant, separately. In Figure 6.6 (a), the COF is determined to decrease with increasing load no matter what the contacting pair is. The COF of the NCD series is higher than that of MCD series under the same conditions. For NCD series, the COF ranges from 0.12 to 0.18 whereas the COF of MCD is less than 0.12. It is notable that very low friction (0.04-0.08) is observed when MCD and MCD-NH_3 were used as mating surface with cartilage. The friction of cartilage-cartilage contact is between the cartilage-NCD contact and the cartilage-MCD contact. Another significant observation is that for both NCD and MCD the functionalization dramatically influences the frictional property. The hydrogen treatment increases the friction between the diamond surface and the cartilage surface. The COF for NCD drops after the ammonia treatment. In the case of MCD, at small load of 0.5 N, the COF decreases a little amount after the functionalization of ammonia. At higher loads, however, the COF becomes higher after the treatment. The measured COF is revealed in Figure 6.6 (b) with the lubrication of calf bovine serum. The COF is found to reduce with load when serum was used as lubricant. Compared to DI water, serum effectively reduces the friction. In the case of NCD-cartilage, the COF reduces to 0.023 at the load of 1.5 N.

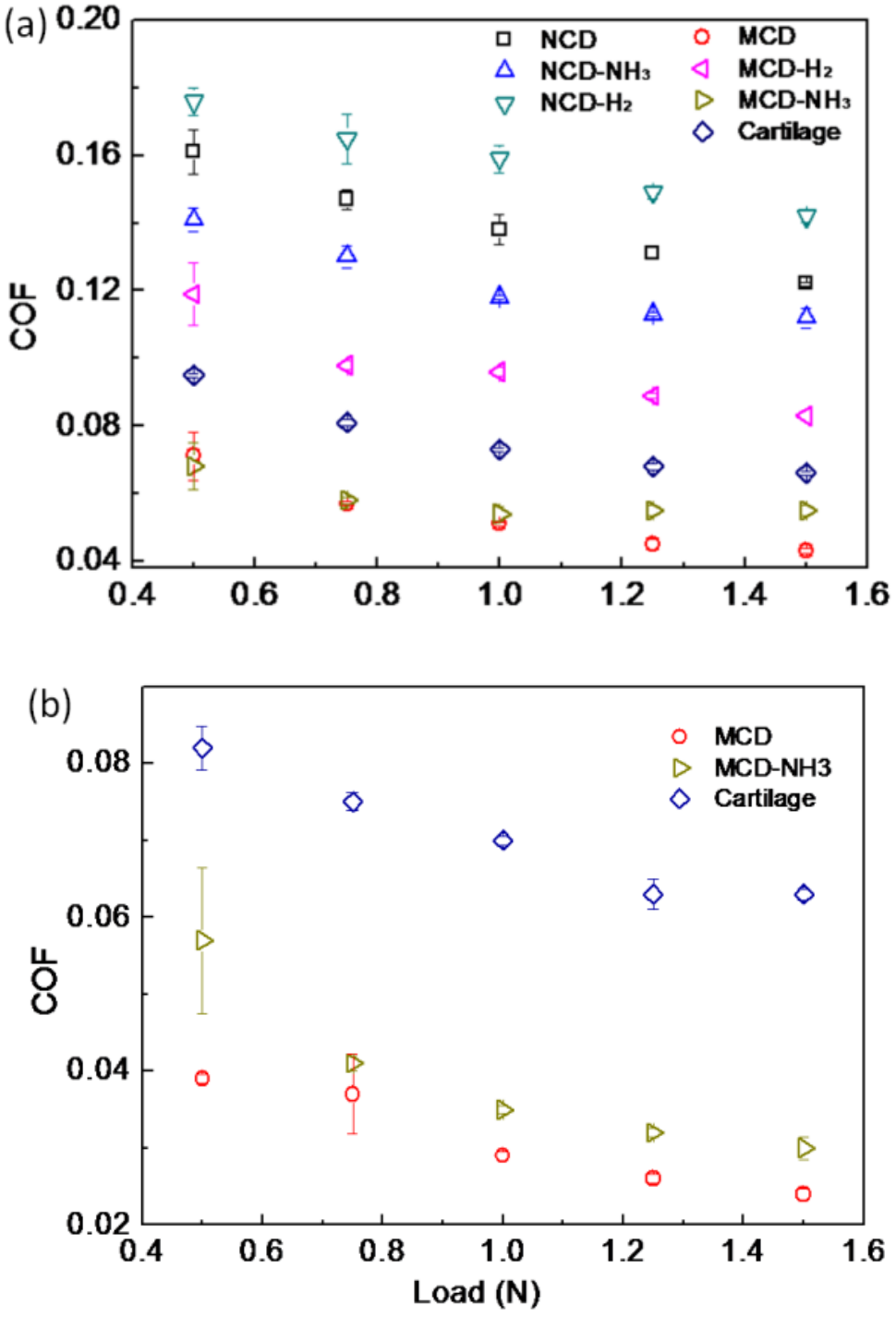

Figure 6.6. Variation of COF with applied load (Sliding speed was fixed at 2.5 mm/s. a, in DI water environment, b, in calf bovine serum environment).

Cartilage has the properties of elastomers[215, 216] which are characterized by viscoelasticity. When sliding against another object under external load, the cartilage produces deformation. The friction force between the cartilage and the object is determined by the combination of the adhesion force and the deformation force.[217] Compared to the strong effect of adhesion, the force induced by deformation is relatively insignificant. Therefore, the adhesion force dominates the frictional force.

According to the classic theory developed by Tabor,[218] the adhesion force is positively related to the actual contact area between the mating surfaces. For both rigid body and elastomer, the real contact area has been found to increase with load in a power law with an index less than 1,[219, 220] $A_r \propto N^x$ (x<1). Dividing the adhesion force by the load generates the COF, $COF \propto A_r/N = N^{x-1}$. The index for the load is less than 0, determining that COF decreases with load. This is the explanation for the decreasing trend of COF in Figure 6.6.

The change of COF with sliding speed is shown in Figure 6.7. Under a constant load, the COF reversely changes with speed in most cases except for the MCD-cartilage contact. The COF for MCD-cartilage contact decreases with speed in DI water environment while it stays stable in serum environment. The impact of functionalization still can be observed in Figure 6.7. Similar to the observation in Figure 6.6, the hydrogen treatment increases the friction and ammonia treatment decreases it for NCD as shown in Figure 6.7 (a).

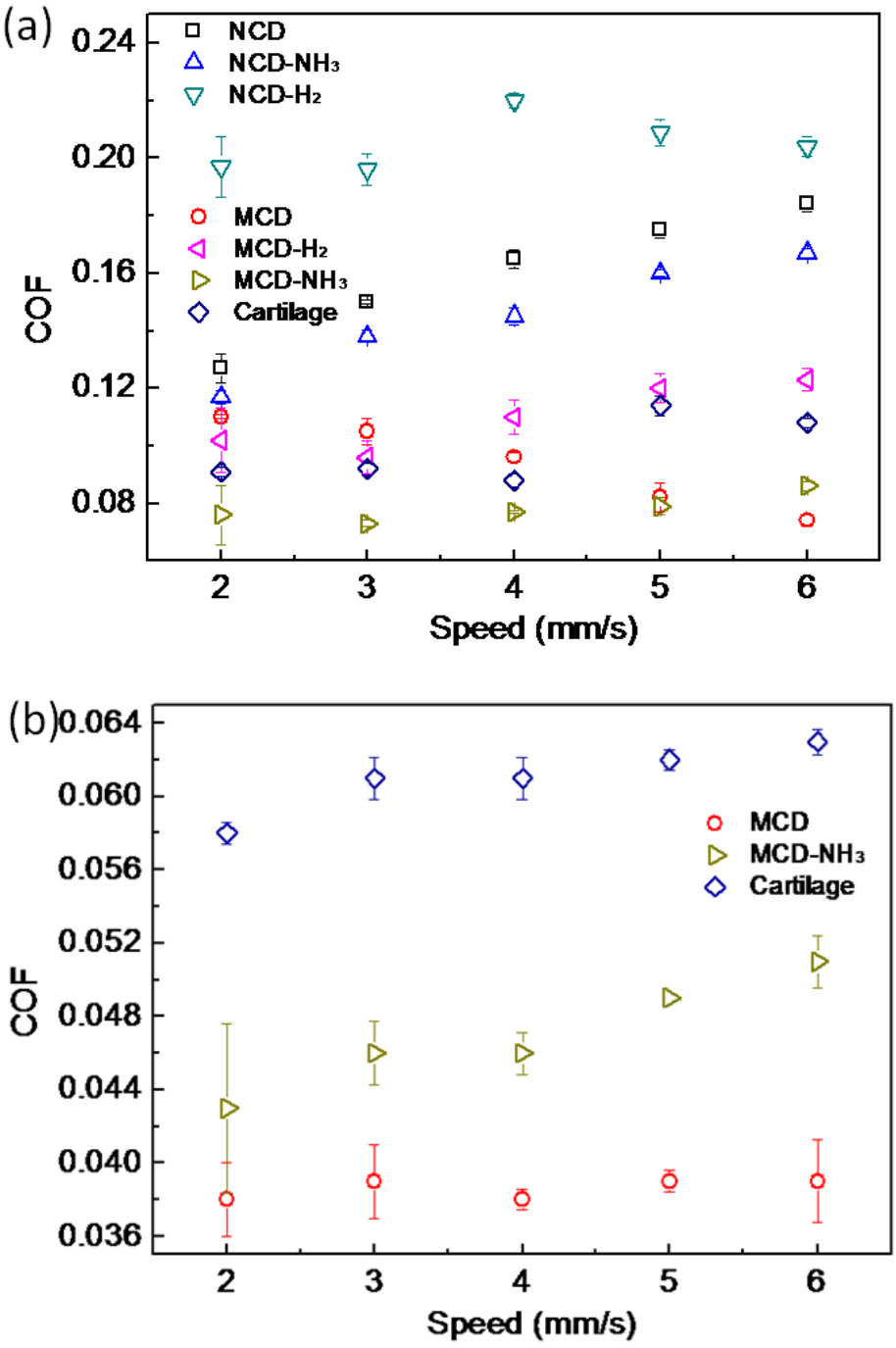

Figure 6.7. Variation of COF with sliding speed (Applied load was fixed at 1 N. a, in DI water environment, b, in calf bovine serum environment).

For MCD, both functionalization methods reduce the friction at low speed while increase that at high speed in DI water environment. When serum was used, the ammonia treatment increases the friction force between the diamond and the cartilage. Compared to the COF ranging from 0.058-0.063 for cartilage-cartilage contact, the COF for MCD-cartilage contact is relatively low (~0.038).

6.5. Surface wear on cartilage

The surface morphology of the cartilage before and after the wear test is displayed in Figure 6.8. There is no clear sign of severe wear by comparing Figure 6.8 (a) and (b). Randomly distributed small bumps can be observed in both figures. These surface textures are analogous to asperities on a rough surface. After the wear test, the bumps maintain their overall shape and were not scratched off. One difference can be seen from the bumps. After wear test, the surface of some bumps becomes flat as shown in the circles. This is believed to result from the plastic deformation of the asperities caused by the normal stress and shear stress in the sliding. The flat surface is not produced through the scratch of material from the top of the bump. The scratch will generate grooves or damaged structure on the surface, which is not seen in Figure 6.8 (b).

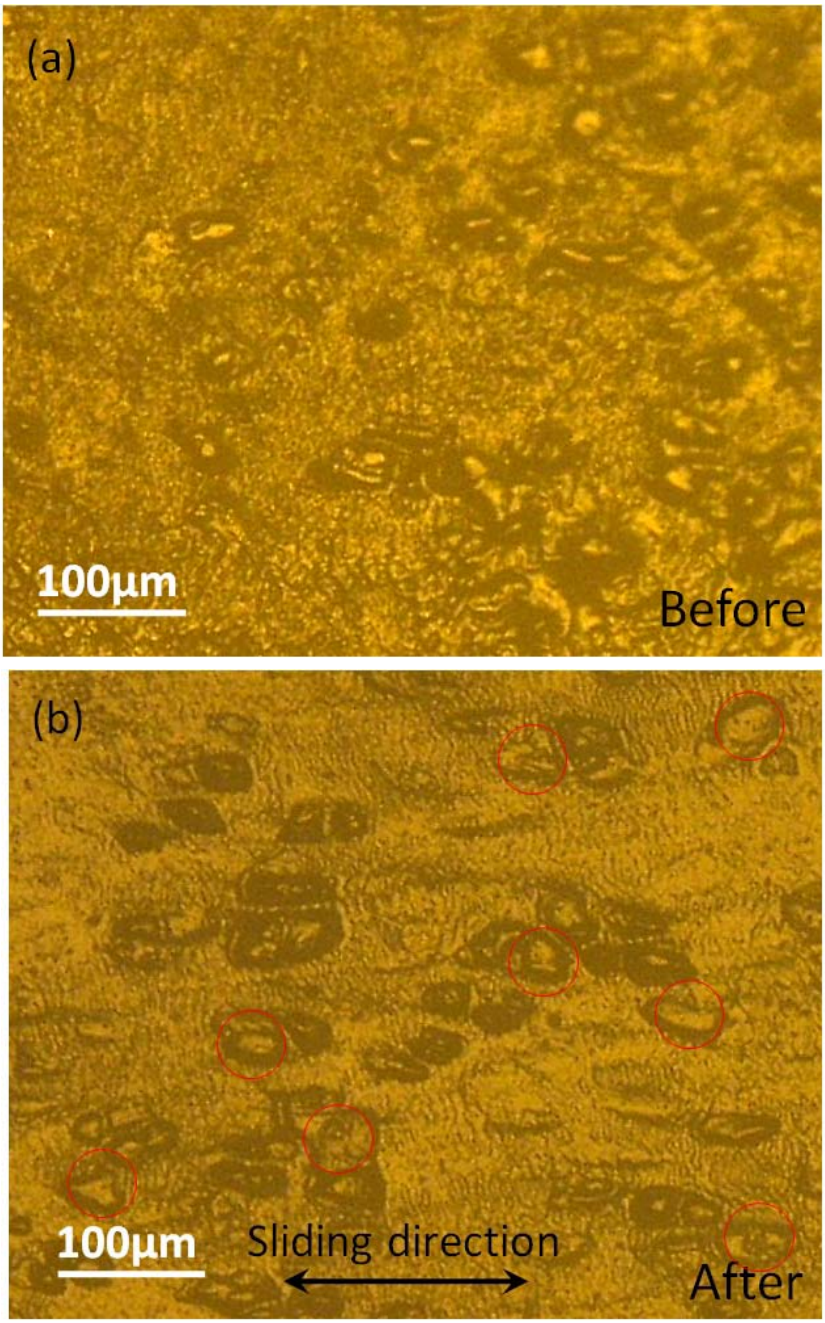

Figure 6.8. Optical microscope image of the cartilage surface before (a) and after (b) the wear test (Cartilage sliding on MCD surface with a fixed load of 1N and fixed speed of 6 mm/s for 2000 cycles in calf bovine serum environment).

6.6. Model of the cartilage-diamond contact

Adhesion force on the diamond samples is determined by the hydrogen bond and the electrostatic interactions between the diamond surface and the proteins of the cartilage. The contact between cartilage protein and diamond surface during sliding at different conditions is schematically displayed in Figure 6.9. In dry conditions, the ammonia treated sample has the most interactions while the density of interactions on the H-terminated diamond is the lowest, so do the adhesion force. With the introduction of lubricant, the scenario changes remarkably. In some regions, lubricant enters the interface and separates the protein and the diamond surface. The interaction still exists in the rest regions. It is apparent that the more areas are occupied by lubricant, the less adhesion is left. The ammonia treated diamond is most hydrophilic and the hydrogen treated diamond has the worst hydrophilicity. Therefore, the sequence of the functionalization methods are ammonia treatment, no treatment and hydrogen treatment in term of surface area affected by the lubrication. Figure 6.9 indicates that the final adhesion is determined by two factors: the surface area occupied by the lubricant and the original density of the interactions established between protein and diamond. In this study, these two factors conflict with each other as shown in the figure. The difference of friction between NCD and MCD can be explained by the lower surface energy of sp^2 bonded carbon. As a result, more interactions can be established and adhesion and friction is higher between NCD and protein. Based on the results of frictional experiment, microcrystalline diamond without functionalization

has the lowest total adhesion, as well as the friction, with cartilage. If this material is utilized as the coating film in the artificial joint, low friction will be achieved and long service life is possible.

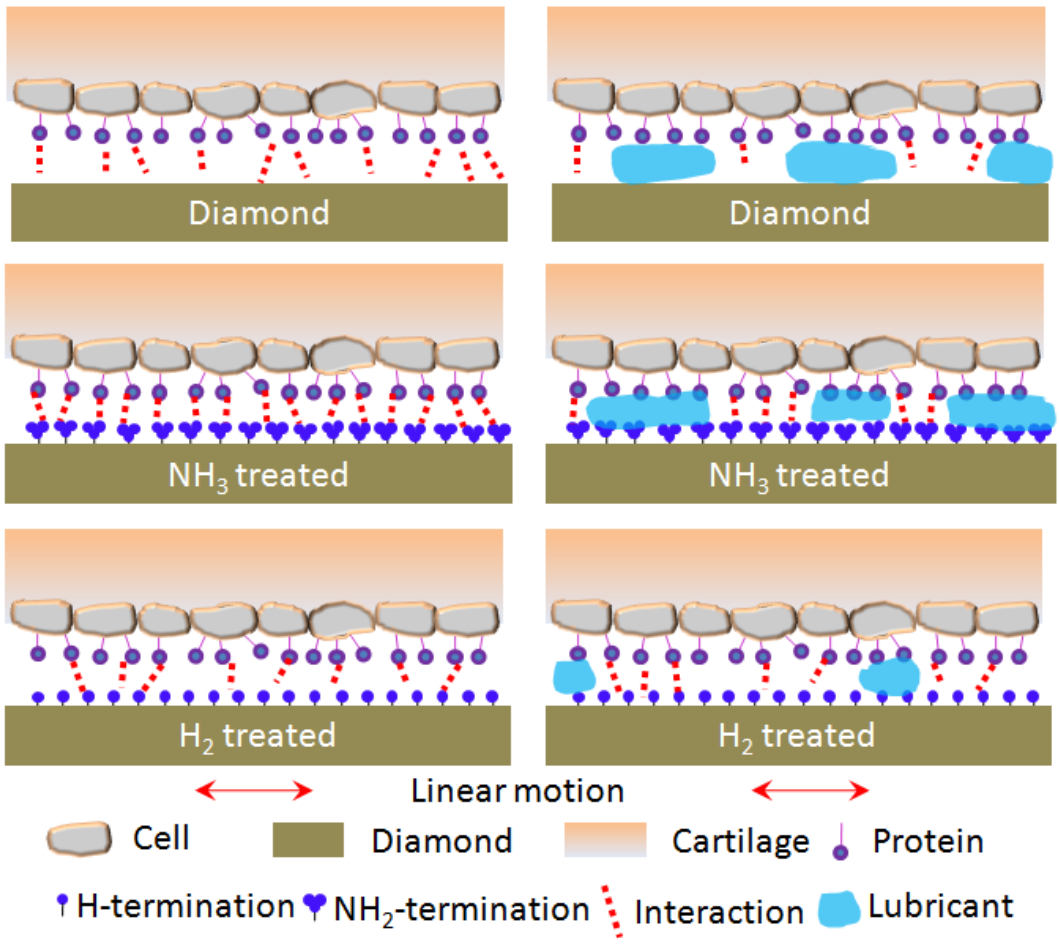

Figure 6.9. Schematic of adhesion during sliding of cartilage on different diamond surfaces. Left column is in dry condition, right column is in lubricated condition. Thickness of dashed line indicates strength of the bond.

6.7. Summary

Tribological study was conducted on six diamond samples which have different surface chemistry and structures. When they were slide against cartilage, the hydrogen treatment was found to increase the friction for both nanocrystalline diamond and microcrystalline diamond. The ammonia treatment reduced the friction for NCD and increased that for MCD. This is due to the synergetic This is due to the synergic effects of the amount of lubricant molecules trapped within the matting surface and the interfacial interactions between protein and diamond surfaces. Compared to cartilage-cartilage contact, the cartilage-MCD has lower COF, indicating that MCD behaves better than nature and this material is promising to be used in artificial joints.

CHAPTER VII

CONCLUSIONS AND RECOMMENDATIONS

7.1. Conclusions

This research studied the tribological and electrochemical properties of diamond-containing materials. Two types of diamond reinforced ceramic composites and six types of diamond coating films were investigated.

The two composites are composed of boron-doped diamond particles, Si and SiC. They were investigated using a tribo-electrochemical approach for *in situ* monitoring of wear. The COF of the DRCC-1, which has with larger diamond grits and higher area fraction of diamond, was much lower than that of the DRCC-2. This was attributed to the lower contact pressure due to higher area fraction of diamond. Two circuit models representing the two composites were developed based on the EIS measurement and simulation. Experimental data revealed the sinusoidal behavior of the current density against potential in Tafel curves. It was correlated to the amorphization-wear process during rubbing. The smaller amplitude in the sinusoidal pattern indicates less intense amorphization-wear process. This behavior was affected by the grit size of diamonds. The larger diamond grit generated less current due to lower wear in comparison with otherwise. These results showed that the wear of the diamond-containing composites can be *in situ* monitored by means of the proposed electrochemical approach. The approach developed in this research could be used for

the monitor, control and management of working tools.

In order to study the wear mechanism of the diamond composite, the worn surface and wear debris after tribological experiments were characterized using Raman spectrometer, SEM, and profilometer. The results showed that the intensity ratio of sp^3 bonded carbon to sp^2 bonded carbon decreased as the wear of diamond particle increased. The phase transformation of diamond carbon to amorphous carbon was confirmed by the decrease of sp^3/sp^2 ratio. In the wear debris, Si was found to transform from crystalline to both amorphous and oxidized structures. The phase transformation weakened the mechanical strength of carbon at the interface. The formation of amorphous silica particles as polishing agent promoted the polishing of diamond that was proved under SEM observation. This was also confirmed by the smoothening and reduction of the surface roughness of diamond particles. The discovery and understanding of diamond polishing mechanism is important for applications industries that use wear components.

Human cartilage was used as counter surface to study the tribological properties of diamond in biomedical applications. Tribological study was conducted on six diamond samples which have different surface functionalization and structures. When slide against cartilage, the hydrogen treatment was found to increase the friction for both nanocrystalline (NCD) and microcrystalline diamond (MCD). The ammonia treatment one, on the other hand, reduced the friction for NCD and increased that for MCD. This was due to the synergic effects of the amount of lubricant molecules trapped within the matting surface and the interfacial interactions between protein and

diamond surfaces. Compared to cartilage-cartilage contact, the cartilage-MCD had lower COF. This proved that the MCD behaved better than nature in terms of surface friction and this material is promising to be used in artificial joints.

The findings in this research provide new understanding of diamond wear and tribological performance of diamond on biomaterial surface. These results are beneficial for the improvement in design of diamond tools to reduce wear, and development of devices for monitoring wear of insulating materials. The applications of diamond in prosthetic and biomedical industries will be broadened as well. The experimental results and discussion in this research are helpful for science and engineering communities who work on the properties and applications of diamond materials.

7.2. Recommendations

Based on the findings in this work, the recommendations for future works are:

1) Study of other diamond structures: Various forms of diamond, such as single crystalline diamond, nanocrystalline diamond and microcrystalline diamond, are currently utilized in industries. The wear mechanism of various types of diamond could be different. In this study, the diamond particle is single crystalline. The wear mechanism of other types of diamond should be investigated in the future.

2) Tribological and electrochemical properties in different chemical environments: Most of the experiments in this research are conducted in aqueous environment. The diamond materials in applications are usually exposed to acid or base solutions. The chemical environment is believed to have great impact on the properties. Therefore, the investigation of diamond materials in different chemical solutions would be interesting.

3) Effect of other functionalization on diamond surface: The surface functionalizaiton has been proved to greatly change the surface properties of diamond. Using other functionalization methods, it is possible to obtain a diamond surface which has even better tribological performance than MCD in this research.

REFERENCES

1. J. Wilks and E. Wilks, *Properties and Applications of Diamond.* (Butterworth-Heinemann, Oxford, 1991).

2. R. F. Davis, *Diamond Films and Coatings.* (Noyes Publications, Park Ridge, IL, 1993).

3. E. Erlich and W. D. Hausel, *Diamond Deposits: Origin, Exploration, and History of Discovery.* (SME, Littleton, CO, 2002).

4. F. Bundy, H. Hall, H. Strong and R. Wentorf, Nature 176 (4471), 51-55 (1955).

5. H. T. Hall, Review of Scientific Instruments 31 (2), 125-131 (2004).

6. A. Giardini, J. Tydings and S. Levin, American Mineral 45, 217-221 (1960).

7. H. T. Hall, Review of Scientific Instruments 29 (4), 267-275 (2004).

8. L. D. Hall, Review of Scientific Instruments 29 (5), 367-370 (2004).

9. R. Wedlake, *The Properties of Diamond.* (Academic Press, London, 1979).

10. H. L. D. Pugh and J. Lees, Nature 191, 865-867 (1961).

11. P. S. DeCarli and J. C. Jamieson, Science 134 (3472), 92-92 (1961).

12. T. Sekine, M. Akaishi, N. Setaka and K.-I. Kondo, Journal of Materials Science 22 (10), 3615-3619 (1987).

13. I. Simonsen, S. Chevacharoenkul, Y. Horie, T. Akashi and H. Sawaoka, Journal of Materials Science 24 (4), 1486-1490 (1989).

14. L. F. Trueb, Journal of Applied Physics 42 (2), 503-510 (2003).

15. L. F. Trueb, Journal of Applied Physics 41 (12), 5029-5030 (2003).

16. L. F. Trueb, Journal of Applied Physics 39 (10), 4707-4716 (2003).

17. I. Simonsen, Y. Horie, T. Akashi and A. Sawaoka, Journal of Materials Science 27 (7), 1735-1740 (1992).

18. G. Burkhard, K. Dan, Y. Tanabe, A. B. Sawaoka and K. Yamada, Japanese Journal of Applied Physics 33 (part 2), L876-L879 (1994).

19. W. Gajewski, P. Achatz, O. Williams, K. Haenen, E. Bustarret, M. Stutzmann and J. A. Garrido, Physical Review B 79 (4), 045206 (2009).

20. R. Wentorf, R. C. DeVries and F. Bundy, Science 208 (4446), 873-880 (1980).

21. S.-J. Li, M. Akaishi, T. Ohsawa and S. Yamaoka, Journal of Materials Science 25 (9), 4150-4156 (1990).

22. M. Akaishi, S. Yamaoka, J. Tanaka, T. Ohsawa and O. Fukunaga, Materials Science and Engineering: A 105, 517-523 (1988).

23. S. Davey, T. Evans and S. Robertson, Journal of Materials Science Letters 3 (12), 1090-1092 (1984).

24. M. Kamo, Y. Sato, S. Matsumoto and N. Setaka, Journal of Crystal Growth 62 (3), 642-644 (1983).

25. S. Matsumoto, Y. Sato, M. Kamo and N. Setaka, Japanese Journal of Applied Physics 21 (4A), L183-L185 (1982).

26. M. Kamo, H. Yurimoto and Y. Sato, Applied Surface Science 33, 553-560 (1988).

27. S. Matsumoto, Journal of Materials Science Letters 4 (5), 600-602 (1985).

28. K. Suzuki, A. Sawabe, H. Yasuda and T. Inuzuka, Applied Physics Letters 50 (12), 728-729 (1987).

29. S. Koizumi, T. Murakami, T. Inuzuka and K. Suzuki, Applied Physics Letters 57 (6), 563-565 (1990).

30. K. Suzuki, A. Sawabe and T. Inuzuka, Japanese Journal of Applied Physics 29 (part 1), 153-157 (1990).

31. A. Sawabe, H. Yasuda, T. Inuzuka and K. Suzuki, Applied Surface Science 33, 539-545 (1988).

32. K. Suzuki, A. Sawabe and T. Inuzuka, Applied Physics Letters 53 (19), 1818-1819 (1988).

33. J. Wei, H. Kawarada, J.-i. Suzuki and A. Hiraki, Journal of Crystal Growth 99 (1), 1201-1205 (1990).

34. P. Hartmann, R. Haubner and B. Lux, Diamond and Related Materials 5 (6), 850-856 (1996).

35. W. Wanlu, L. Kejun, G. Jinying and L. Aimin, Thin Solid Films 215 (2), 174-178 (1992).

36. N. Glumac and D. Goodwin, Combustion and Flame 105 (3), 321-331 (1996).

37. D. Goodwin, N. Glumac and H. Shin, presented at the Symposium (International) on Combustion, 1996 (unpublished).

38. S. J. Harris, H. S. Shin and D. G. Goodwin, Applied Physics Letters 66 (7), 891-893 (1995).

39. B. Ruf, F. Behrendt, O. Deutschmann, S. Kleditzsch and J. Warnatz, Proceedings of the Combustion Institute 28 (1), 1455-1461 (2000).

40. C. Li, R. Zhu, J. Liu, L. Chen, J. Guo, C. Hua, L. Hei, J. Wei, J. Wang and Z. Feng, Diamond and Related Materials 39, 47-52 (2013).

41. J. Liu, L. Hei, G. Chen, C. Li, J. Song and F. Lu, Surface and Coatings Technology 236, 8-12 (2013).

42. J. C. Angus and H. Will, Journal of Applied Physics 39 (6), 2915-2922 (1968).

43. B. Deryagin and D. Fedoseev, Russian Chemical Reviews 39 (9), 783-788 (1970).

44. L. Holland and S. Ojha, Thin Solid Films 58 (1), 107-116 (1979).

45. K. Nishimura, K. Das and J. Glass, Journal of Applied Physics 69 (5), 3142-3148 (1991).

46. T. R. Anthony, *The Physics and Chemistry of Carbides, Nitrides and Borides* (Springer, Berlin, 1990).

47. M. Kamo, S. Matsumoto, Y. Sato and N. Setaka, U.S. patent 4434188 A (1984). http://www.google.com/patents/US4434188

48. S. Koizumi, M. Kamo, Y. Sato, H. Ozaki and T. Inuzuka, Applied Physics Letters 71 (8), 1065-1067 (1997).

49. A. Voevodin, S. Walck and J. Zabinski, Wear 203, 516-527 (1997).

50. W. Liu, C.-X. Luo, J.-X. Yan and T.-M. Zhang, Integrated Ferroelectrics 150 (1), 137-146 (2014).

51. B. M. Moshtaghioun, A. L. Ortiz, D. Gómez-García and A. Domínguez-Rodríguez, Journal of the European Ceramic Society 33 (8), 1395-1401 (2013).

52. B. Bhushan, Diamond and Related Materials 8 (11), 1985-2015 (1999).

53. J. Yang, H. Sun and C. Chen, Journal of the American Chemical Society 130 (23), 7200-7201 (2008).

54. L. Wei, P. Kuo, R. Thomas, T. Anthony and W. Banholzer, Physical Review Letters 70 (24), 3764-3767 (1993).

55. T. Anthony, W. Banholzer, J. F. Fleischer, L. Wei, P. Kuo, R. Thomas and R. Pryor, Physical Review B 42 (2), 1104-1111 (1990).

56. J. Che, T. Çağın, W. Deng and W. A. Goddard III, The Journal of Chemical Physics 113 (16), 6888-6900 (2000).

57. P. H. Chen, C. L. Lin, Y. Liu and C.-Y. Liu, Photonics Technology Letters, IEEE 20 (10), 845-847 (2008).

58. K. Jagannadham, Solid-State Electronics 42 (12), 2199-2208 (1998).

59. M. Seelmann-Eggebert, P. Meisen, F. Schaudel, P. Koidl, A. Vescan and H. Leier, Diamond and Related Materials 10 (3), 744-749 (2001).

60. H. McSkimin and P. Andreatch Jr, Journal of Applied Physics 43 (7), 2944-2948 (2003).

61. N. Savvides and T. Bell, Thin Solid Films 228 (1), 289-292 (1993).

62. M. Liu, V. I. Artyukhov, H. Lee, F. Xu and B. I. Yakobson, ACS nano 7 (11), 10075-10082 (2013).

63. F. P. Bundy, H. P. Bovenkerk, H. M. Strong and R. H. Wentorf Jr, The Journal of Chemical Physics 35 (2), 383-391 (2004).

64. C. Brookes and E. Brookes, Diamond and Related Materials 1 (1), 13-17 (1991).

65. J. E. Field, *The Properties of Natural and Synthetic Diamond.* (Academic Press, London, 1992).

66. K. Shibuki, M. Yagi, K. Saijo and S. Takatsu, Surface and Coatings Technology 36 (1), 295-302 (1988).

67. K. H. Kim, N. Moldovan, C. Ke, H. D. Espinosa, X. Xiao, J. A. Carlisle and O. Auciello, Small 1 (8-9), 866-874 (2005).

68. H. Sumiya, K. Harano and T. Irifune, Review of Scientific Instruments 79 (5), 056102-056103 (2008).

69. C. Donnet and A. Grill, Surface and Coatings Technology 94, 456-462 (1997).

70. Y. Mabuchi, T. Higuchi, Y. Inagaki, H. Kousaka and N. Umehara, Wear 298, 48-56 (2013).

71. H. Abdullah Tasdemir, M. Wakayama, T. Tokoroyama, H. Kousaka, N. Umehara, Y. Mabuchi and T. Higuchi, Wear 307 (1), 1-9 (2013).

72. A. R. Konicek, D. Grierson, P. Gilbert, W. Sawyer, A. Sumant and R. W. Carpick, Physical Review Letters 100 (23), 235502-1-235502-4 (2008).

73. B. Podgornik, D. Hren and J. Vižintin, Thin Solid Films 476 (1), 92-100 (2005).

74. B. Podgornik and J. Vižintin, Surface and Coatings Technology 200 (5), 1982-1989 (2005).

75. B. Podgornik, M. Sedlaček and J. Vižintin, Tribology International 41 (6), 564-570 (2008).

76. Z. Feng, Y. Tzeng and J. Field, Journal of Physics D: Applied Physics 25 (10), 1418-1424 (1992).

77. F. Cui and D. Li, Surface and Coatings Technology 131 (1), 481-487 (2000).

78. R. K. Roy and K. R. Lee, Journal of Biomedical Materials Research Part B: Applied Biomaterials 83 (1), 72-84 (2007).

79. L. Anne Thomson, F. C. Law, N. Rushton and J. Franks, Biomaterials 12 (1), 37-40 (1991).

80. R. Butter, M. Allen, L. Chandra, A. Lettington and N. Rushton, Diamond and Related Materials 4 (5), 857-861 (1995).

81. T. Das, D. Ghosh, T. Bhattacharyya and T. Maiti, Journal of Materials Science: Materials in Medicine 18 (3), 493-500 (2007).

82. K. Gutensohn, C. Beythien, J. Bau, T. Fenner, P. Grewe, R. Koester, K. Padmanaban and P. Kuehnl, Thrombosis Research 99 (6), 577-585 (2000).

83. T. Strother, T. Knickerbocker, J. N. Russell, J. E. Butler, L. M. Smith and R. J. Hamers, Langmuir 18 (4), 968-971 (2002).

84. C. G. Specht, O. A. Williams, R. B. Jackman and R. Schoepfer, Biomaterials 25 (18), 4073-4078 (2004).

85. K. Saijo, M. Yagi, K. Shibuki and S. Takatsu, Surface and Coatings Technology 43, 30-40 (1990).

86. J. Arsecularatne, L. Zhang and C. Montross, International Journal of Machine Tools and Manufacture 46 (5), 482-491 (2006).

87. X. Ding, W. Liew and X. Liu, Wear 259 (7), 1225-1234 (2005).

88. M. Ramulu, M. Faridnia, J. Garbini and J. Jorgensen, Journal of Engineering Materials and Technology 113 (4), 430-436 (1991).

89. C. Nath, M. Rahman and K. S. Neo, International Journal of Machine Tools and Manufacture 49 (14), 1089-1095 (2009).

90. J. Paulo Davim and A. Monteiro Baptista, Journal of Materials Processing Technology 103 (3), 417-423 (2000).

91. R. Coelho, S. Yamada, D. Aspinwall and M. Wise, International Journal of Machine Tools and Manufacture 35 (5), 761-774 (1995).

92. S. Ederyd, S. M. Packer, G. Rai and A. A. Rodriguez, U.S. patent 5697994 A

(1997). http://www.google.com/patents/US5697994

93. R. Teti, CIRP Annals-Manufacturing Technology 51 (2), 611-634 (2002).

94. H. Suzuki, T. Moriwaki, Y. Yamamoto and Y. Goto, CIRP Annals-Manufacturing Technology 56 (1), 131-134 (2007).

95. F. Mata, V. Gaitonde, S. Karnik and J. P. Davim, Journal of Materials Processing Technology 209 (4), 1980-1987 (2009).

96. F. Nabhani, Journal of Materials Processing Technology 115 (3), 402-412 (2001).

97. P. J. Heath, Journal of Materials Processing Technology 116 (1), 31-38 (2001).

98. E. Kuljanic, M. Fioretti, L. Beltrame and F. Miani, CIRP Annals-Manufacturing Technology 47 (1), 61-64 (1998).

99. S. Huang, L. Zhou, J. Chen and L. Xu, Materials and Manufacturing Processes 27 (10), 1090-1094 (2012).

100. C. J. Andrewes, H.-Y. Feng and W. Lau, Journal of Materials Processing Technology 102 (1), 25-29 (2000).

101. J. P. Davim, Journal of Materials Processing Technology 128 (1), 100-105 (2002).

102. B. Guo, Q. Zhao and X. Fang, Journal of Materials Processing Technology 214 (5), 1045-1051 (2014).

103. P. Koshy, A. Iwasald and M. Elbestawl, CIRP Annals-Manufacturing Technology 52 (1), 271-274 (2003).

104. Q. Zhao, Y. Liang, D. Stephenson and J. Corbett, International Journal of Machine Tools and Manufacture 47 (14), 2091-2097 (2007).

105. T. Hantschel, P. Niedermann, T. Trenkler and W. Vandervorst, Applied Physics Letters 76 (12), 1603-1605 (2000).

106. T. Shibata, K. Unno, E. Makino and S. Shimada, Sensors and Actuators A: Physical 114 (2), 398-405 (2004).

107. J. Bae, T. Ono and M. Esashi, Diamond and Related Materials 12 (12), 2128-2135 (2003).

108. B. Mesa and S. Magonov, presented at the Journal of Physics: Conference Series, 2007 (unpublished).

109. H. Sumiya, Review of Scientific Instruments 76 (2), 026112-1-026112-3 (2005).

110. A. Noreyan, J. Amar and I. Marinescu, Materials Science and Engineering: B 117 (3), 235-240 (2005).

111. K. Herrmann, N. Jennett, W. Wegener, J. Meneve, K. Hasche and R. Seemann, Thin Solid Films 377, 394-400 (2000).

112. P. Niedermann, W. Hänni, N. Blanc, R. Christoph and J. Burger, Journal of Vacuum Science & Technology A 14 (3), 1233-1236 (1996).

113. P. Gallo, A. Kulik, N. Burnham, F. Oulevey and G. Gremaud, Nanotechnology 8 (1), 10-13 (1997).

114. M. Mohanty, T. Anilkumar, P. Mohanan, C. Muraleedharan, G. Bhuvaneshwar, F. Derangere, Y. Sampeur and R. Suryanarayanan, Biomolecular Engineering 19 (2), 125-128 (2002).

115. K. F. Chong, K. P. Loh, S. Vedula, C. T. Lim, H. Sternschulte, D. Steinmüller, F.-s. Sheu and Y. L. Zhong, Langmuir 23 (10), 5615-5621 (2007).

116. R. Hauert, L. Knoblauch-Meyer, G. Francz, A. Schroeder and E. Wintermantel, Surface and Coatings Technology 120, 291-296 (1999).

117. A. Dorner-Reisel, C. Schürer, G. Irmer and E. Müller, Surface and Coatings Technology 177, 830-837 (2004).

118. V.-M. Tiainen, Diamond and Related Materials 10 (2), 153-160 (2001).

119. D. Sheeja, B. Tay and L. Nung, Surface and Coatings Technology 190 (2), 231-237 (2005).

120. K. Holmberg, P. Andersson and A. Erdemir, Tribology International 47, 221-234 (2012).

121. E. Rabinowicz, *Friction and Wear of Materials.* (Wiley, New York, 1965).

122. F. Bowden and D. Tabor, *The Friction and Lubrication of Solids, Part I,* (Oxford University Press, Oxford, 1950).

123. H. Ernst and M. E. Merchant, presented at the Proceedings of MIT Conference on Friction and Surface Finish, 1940 (unpublished).

124. M. C. Shaw and E. F. Macks, *Analysis and Lubrication of Bearings.* (McGraw-Hill Book Co., New York, 1949).

125. N. P. Suh and H.-C. Sin, Wear 69 (1), 91-114 (1981).

126. H. Meng and K. Ludema, Wear 181, 443-457 (1995).

127. J. Challen and P. Oxley, Wear 53 (2), 229-243 (1979).

128. D. Tabor, Journal of Lubrication Technology 103 (2), 169-179 (1981).

129. G. He, M. H. Müser and M. O. Robbins, Science 284 (5420), 1650-1652 (1999).

130. Y. Mo, K. T. Turner and I. Szlufarska, Nature 457 (7233), 1116-1119 (2009).

131. M. Cieplak, E. D. Smith and M. O. Robbins, Science 265 (5176), 1209-1212 (1994).

132. J. Krim, Surface Science 500 (1), 741-758 (2002).

133. B. Bhushan and S. Sundararajan, Acta Materialia 46 (11), 3793-3804 (1998).

134. D. Rigney and J. Hirth, Wear 53 (2), 345-370 (1979).

135. B. J. Briscoe and D. Tabor, British Polymer Journal 10 (1), 74-78 (1978).

136. R. Bowers, W. Clinton and W. A. Zisman, *Frictional Behavior of Polyethylene, Polytetrafluoroethylene, and Halogenated Derivatives.* (Technical report published by Naval Research Lab, Report Number: NRL-4167, Washington, DC, 1953).

137. D. F. Moore, *The Friction and Lubrication of Elastomers.* (Pergamon Press, Oxford, 1972).

138. C. M. Pooley and D. Tabor, Proceedings of the Royal Society of London. Series A, Mathematical and Physical Sciences 329, 251-274 (1972).

139. R. Steijn, Wear 12 (3), 193-212 (1968).

140. J. Challen, P. Oxley and B. Hockenhull, Wear 111 (3), 275-288 (1986).

141. K. Mao, Wear 262 (11), 1281-1288 (2007).

142. I. Kraghelsky and E. Nepomnyashchi, Wear 8 (4), 303-319 (1965).

143. T. Saito, T. Hosoe and F. Honda, Wear 247 (2), 223-230 (2001).

144. M. Hitchiner and J. Wilks, Wear 93 (1), 63-80 (1984).

145. J. Vleugels and O. Van der Biest, Wear 225, 285-294 (1999).

146. R. Montgomery, Wear 8 (4), 289-302 (1965).

147. P. Kodali, K. Walter and M. Nastasi, Tribology International 30 (8), 591-598 (1997).

148. H. Ronkainen, S. Varjus and K. Holmberg, Wear 222 (2), 120-128 (1998).

149. J. Hu, Y. Chou, R. Thompson, J. Burgess and S. Street, Surface and Coatings Technology 202 (4), 1113-1117 (2007).

150. J. P. Davim and F. Mata, Materials & Design 29 (8), 1568-1574 (2008).

151. P. U. Arumugam, A. P. Malshe and S. A. Batzer, Surface and Coatings Technology 200 (11), 3399-3403 (2006).

152. K. Ding, Y. Fu, H. Su, X. Gong and K. Wu, The International Journal of Advanced Manufacturing Technology 71, 1929-1938 (2014).

153. M. Hitchiner and J. Wilks, Wear 114 (3), 327-338 (1987).

154. K.-H. Chung and D.-E. Kim, Ultramicroscopy 108 (1), 1-10 (2007).

155. J. Liu, D. Grierson, N. Moldovan, J. Notbohm, S. Li, P. Jaroenapibal, S. O'Connor, A. Sumant, N. Neelakantan and J. Carlisle, Small 6 (10), 1140-1149 (2010).

156. J. Liu, J. K. Notbohm, R. W. Carpick and K. T. Turner, ACS nano 4 (7), 3763-3772 (2010).

157. Y. Zhang, Y. Zhang, H. Tang and L. Wang, The International Journal of Advanced Manufacturing Technology 48 (5-8), 455-460 (2010).

158. G. Byrne, D. Dornfeld, I. Inasaki, G. Ketteler, W. König and R. Teti, CIRP Annals-Manufacturing Technology 44 (2), 541-567 (1995).

159. Y. Wong, A. Nee, X. Li and C. Reisdorf, Journal of Materials Processing Technology 63 (1), 205-210 (1997).

160. F. Luk, V. Huynh and W. North, Journal of Physics E: Scientific Instruments 22 (12), 977 (1989).

161. R. Du, B. Zhang, W. Hungerford and T. Pryor, ASME-PUBLICATIONS-PED 63, 245-245 (1993).

162. S. Damodarasamy and S. Raman, Computers in Industry 16 (1), 25-34 (1991).

163. L. Lee, K. Lee and C. Gan, International Journal of Machine Tools and Manufacture 29 (3), 295-303 (1989).

164. A. Sarhan, R. Sayed, A. Nassr and R. El-Zahry, Journal of Materials Processing Technology 109 (3), 229-235 (2001).

165. S. Choudhury and K. Kishore, International Journal of Machine Tools and Manufacture 40 (6), 899-909 (2000).

166. J. Tlusty and G. Andrews, CIRP Annals-Manufacturing Technology 32 (2), 563-572 (1983).

167. B. Lindstrom and B. Lindberg, presented at the Proc. 24th. Int. Machine Tool Design and Research Conf, 1983 (unpublished).

168. H. Takeyama, Y. Doi, T. Mitsuoka and H. Sekiguchi, Bulletin of JSME 12 (49), 132-140 (1969).

169. T. Stoferle and B. Bellmann, presented at the Proceeding of 16th International Machine Tool Design and Research Conference, 1975 (unpublished).

170. D. Dornfeld and E. Kannatey-Asibu, International Journal of Mechanical

Sciences 22 (5), 285-296 (1980).

171. J. M. Fildes, Sensors 9 (1), 11-19 (1991).

172. S. Rangwala and D. Dornfeld, *Intelligent and Integrated Manufacturing Analysis and Synthesis,* (ASME, New York, 1987).

173. R. Du, M. Elbestawi and S. Wu, Journal of Engineering for Industry 117 (2), 121-132 (1995).

174. R. Du, M. Elbestawi and S. Wu, Journal of Engineering for Industry 117 (2), 133-141 (1995).

175. F. Gao and H. Liang, Electrochimica Acta 54 (27), 6808-6815 (2009).

176. F. Gao and H. Liang, Journal of The Electrochemical Society 156 (1), H80-H86 (2009).

177. F. Gao and H. Liang, Journal of Electronic Materials 41 (3), 624-631 (2012).

178. S. Joo and H. Liang, Electrochimica Acta 99, 133-137 (2013).

179. S. Joo and H. Liang, Journal of Electronic Materials 42 (6), 979-987 (2013).

180. J. Liu, C. Li, J. Guo, R. Zhu, L. Chen, J. Wei, L. Hei, J. Wang, Z. Feng and H. Guo, Applied Surface Science 287, 304-310 (2013).

181. H. Xiao, A. M. Sinyukov, X. He, C. Lin and H. Liang, Journal of Applied Physics 114 (22), 223505-1-223505-5 (2013).

182. L. Pastewka, S. Moser, P. Gumbsch and M. Moseler, Nature Materials 10 (1), 34-38 (2011).

183. A. Voevodin, A. Phelps, J. Zabinski and M. Donley, Diamond and Related Materials 5 (11), 1264-1269 (1996).

184. S. Bhattacharyya and S. Silva, Thin Solid Films 482 (1), 94-98 (2005).

185. E. Staryga and G. Bąk, Diamond and Related Materials 14 (1), 23-34 (2005).

186. J. Tafel, Z. Phys. Chem 50, 641-712 (1905).

187. J. Randles, Discussions of the Faraday Society 1, 11-19 (1947).

188. M. E. Orazem and B. Tribollet, *Electrochemical Impedance Spectroscopy.* (John Wiley & Sons, Hoboken, NJ, 2011).

189. C. Chiu, X. He and H. Liang, Electrochimica Acta 94, 42-48 (2013).

190. D. E. Yates, S. Levine and T. W. Healy, Journal of the Chemical Society, Faraday Transactions 1: Physical Chemistry in Condensed Phases 70, 1807-1818 (1974).

191. C.-W. Chiu, J. M. González, M. Harlow and S. B. Vinson, Electrochimica Acta 68, 81-87 (2012).

192. R. Nemanich and S. Solin, Physical Review B 20 (2), 392-401 (1979).

193. L. Liu, X. Wu, Z. Zhang, T. Li and P. K. Chu, Applied Physics Letters 95 (9), 093109-1-093109-3 (2009).

194. C.-C. Chang, H. Chen, C.-C. Chen, W.-H. Hung, I.-K. Hsu, J. Theiss, C. Zhou and S. B. Cronin, Nanotechnology 22 (30), 305709 (2011).

195. B. Li, D. Yu and S.-L. Zhang, Physical Review B 59 (3), 1645-1648 (1999).

196. X.-Z. Zhao, K. Cherian, R. Roy and W. B. White, Journal of Materials Research 13 (7), 1974-1976 (1998).

197. J. Robertson, Progress in Solid State Chemistry 21 (4), 199-333 (1991).

198. J. Robertson, Pure and Applied Chemistry 66 (9), 1789-1796 (1994).

199. A. Ferrari and J. Robertson, Physical Review B 61 (20), 14095 (2000).

200. S. Bhattacharyya, C. Cardinaud and G. Turban, Journal of Applied Physics 83 (8), 4491-4500 (1998).

201. J. Schwan, V. Batori, S. Ulrich, H. Ehrhardt and S. Silva, Journal of Applied Physics 84 (4), 2071-2081 (1998).

202. G. Mariotto, F. Freire Jr and C. Achete, Thin Solid Films 241 (1), 255-259 (1994).

203. M. Tamor and W. Vassell, Journal of Applied Physics 76 (6), 3823-3830 (1994).

204. T. Le Huu, H. Zaidi, D. Paulmier and P. Voumard, Thin Solid Films 290, 126-130 (1996).

205. H. Eyring, The Journal of Chemical Physics 4 (4), 283-291 (2004).

206. F. Tanaka, T. Okabe, H. Okuda, M. Ise, I. A. Kinloch, T. Mori and R. J. Young, Carbon 52, 372-378 (2013).

207. Z. Li, R. J. Young and I. A. Kinloch, ACS Applied Materials & Interfaces 5 (2), 456-463 (2013).

208. K. Wang, H. Liang, J. M. Martin and T. Le Mogne, Applied Physics Letters 91 (5), 051918 (2007).

209. Y. Liu, Y. Tzeng, C. Liu, P. Tso and I. Lin, Diamond and Related Materials 13 (10), 1859-1864 (2004).

210. V. N. Mochalin, O. Shenderova, D. Ho and Y. Gogotsi, Nature Nanotechnology 7 (1), 11-23 (2012).

211. H. Kuzmany, R. Pfeiffer, N. Salk and B. Günther, Carbon 42 (5), 911-917 (2004).

212. L. Ostrovskaya, V. Perevertailo, V. Ralchenko, A. Dementjev and O. Loginova, Diamond and Related Materials 11 (3), 845-850 (2002).

213. J. Hansen, R. Copperthwaite, T. Derry and J. Pratt, Journal of Colloid and Interface Science 130 (2), 347-358 (1989).

214. L. Ostrovskaya, V. Perevertailo, V. Ralchenko, A. Saveliev and V. Zhuravlev, Diamond and Related Materials 16 (12), 2109-2113 (2007).

215. Y. Kang, J. Yang, S. Khan, L. Anissian and G. A. Ameer, Journal of Biomedical Materials Research Part A 77 (2), 331-339 (2006).

216. S.-L. Chia, K. Gorna, S. Gogolewski and M. Alini, Tissue Engineering 12 (7), 1945-1953 (2006).

217. F. P. Bowden and D. Tabor, *The Friction and Lubrication of Solids*. (Oxford University Press, Oxford, 2001).

218. B. Briscoe and D. Tabor, The Journal of Adhesion 9 (2), 145-155 (1978).

219. H. Xiao, D. Guo, S. Liu, G. Pan and X. Lu, Applied Surface Science 258 (8), 3888-3896 (2012).

220. H. Xiao, N. Ariyasinghe, X. He and H. Liang, Colloids and Surfaces B: Biointerfaces (2013).